A comparison of the Minimum Current Corona to a magnetohydrodynamic simulation of quasi-static coronal evolution

D.W. Longcope and T. Magara[1]

Department of Physics, Montana State University
Bozeman, Montana

Draft: February 25, 2004

ABSTRACT

We use two different models to study the evolution of the coronal magnetic field which results from a simple photospheric field evolution. The first, the Minimum Current Corona (MCC), is a self-consistent model for quasi-static evolution which yields an analytic expression approximating the net coronal currents and the free magnetic energy stored by them. For the second model calculation, the non-linear, time-dependent equations of ideal magnetohydrodynamics are solved numerically subject to line-tied photospheric boundary conditions. In both models high current-density concentrations form vertical sheets along the magnetic separator. The time history of the net current carried by these concentrations is quantitatively similar in each of the models. The magnetic energy of the line-tied simulation is significantly greater than that of the MCC, in accordance with the fact that the MCC is a lower bound on energies of all ideal models. The difference in energies can be partially explained from the different magnetic helicity injection in the two models. This study demonstrates that the analytic MCC model accurately predicts the locations of significant equilibrium current accumulations. The study also provides one example in which the energetic contributions of two different MHD constraints, line-tying constraints and flux constraints, may be quantitatively compared. In this example line-tying constraints store at least an order of magnitude more energy than do flux constraints.

Subject headings: MHD — Sun: corona — Sun: magnetic fields

---

[1]Present address: E. O. Hulburt Center for Space Research, Naval Research Laboratory, Washington, DC 20375-5352

1. Introduction

The low solar corona is a strongly magnetized ($\beta \ll 1$) plasma with extremely high resistivity ($Rm \gg 1$). Sequential coronal images made in soft X-ray or extreme ultraviolet reveal only minor changes in much of the low corona over times far greater than typical Alfvén wave transit time. For these reasons it is commonly believed that the coronal magnetic field is in force-free magnetic equilibrium most of the time (Gold & Hoyle 1960; Gold 1964). It is further assumed that this field is "anchored" to the photosphere where magnetic field is confined to localized regions by plasma pressure and convection-driven flows. The photospheric flux evolves slowly, thereby causing the coronal field to change in response. This leads to the widely-held picture that the coronal field evolves quasi-statically in response to photospheric driving.

Non-resitive (ideal), quasi-static evolution driven by footpoint motion will naturally increase the magnetic energy of the coronal field. This energy storage process has been investigated in numerous two-dimensional models (Low 1977; Mikic et al. 1988; Klimchuk et al. 1988). Due to the difficulty in treating realistic three dimensional geometries (it is especially difficult analytically) analogous models are not often applied to observations. As a result, while it is conceded that photospheric motions are generally sufficient to power observed coronal activity (Gold & Hoyle 1960), the power cannot be quantified in specific cases.

In a complete model of coronal activity the magnetic energy which has been slowly stored by photospheric motion must be rapidly *released* (converted from magnetic energy to other forms such as kinetic energy of bulk motion) and then *dissipated* (converted to heat or radiation). Modeling this rapid release, following slow storage, has proven to be a major challenge for coronal physics (see Klimchuk 2001, for a lucid review of various models of storage and release in coronal mass ejections). Magnetic reconnection was invoked as a mechanism of energy dissipation and release by Sweet (1958a) and Parker (1957) in pioneering work. Much of the theoretical investigation which followed this has focused on the local geometry of the reconnection region, and thus is difficult to reconcile with inherently global models of energy storage. In recent theories of fast reconnection, non-ideal effects are very localized, and therefore dissipate negligible energy directly (Biskamp & Schwarz 2001). Without a global context it is not clear how such a localized reconnection process can release so much more energy than it can dissipate. How can energy which is stored throughout the coronal volume be released by reconnection in a tiny region, through which passes only a small fraction of the field lines?

The Minimum Current Corona (MCC, Longcope 1996, 2001) is a recent, self-consistent, analytic model of quasi-static evolution in three-dimensional magnetic fields of arbitrary

complexity. The model simplifies the full equations of ideal magnetohydrodynamics (MHD) using two basic assumptions. Its first assumption, *the discrete-source assumption*, holds that the photospheric field comprises isolated unipolar sources separated by a contiguous region of zero vertical flux (the sources *need not* be point charges, but in many applications they are). As a direct consequence of the discrete-source assumption each coronal field line may be assigned to one of a countable set of *flux domains* according to the source regions at each of its two footpoints. The interfaces between domains are *separatrices*, which intersect along *separators*. Together the separatrices and separators form the *skeleton* of the field (Priest et al. 1997; Longcope & Klapper 2002) which describes the field's connectivity. The number of field lines connecting photospheric sources Pi and Nj is quantified by the magnetic flux in that domain, called the *domain flux* ψ_{ij}.

The second assumption of the MCC, *the FCE-assumption*, is that the corona evolves quasi-statically through a sequence of force-free states called *flux constrained equilibria* (FCEs). A flux constrained equilibrium is that field with the lowest magnetic energy which both matches the photospheric boundary and contains a prescribed distribution of domain fluxes (Longcope & Klapper 2002). Remarkably, the field resulting from this minimization is current-free with the exception of current sheets along each and every one of the field's separators (Longcope 2001).

The MCC assumes, in particular, that the coronal field evolves through those FCEs which hold all domain fluxes constant even as the photospheric flux distribution changes. This evolution is consistent with ideal MHD for some finite plasma velocity, since there is no need for field lines to change topologically or move at infinite speed as they would if footpoints jumped between source regions (Longcope & Cowley 1996). The evolution does require specific footpoint motions *within* each source region which would, in general, differ from any specified photospheric motions. Therefore, *the MCC is inconsistent with the assumption of photospheric line tying.*[1]

Line tying assumes that both footpoints of each field line are frozen to the photosphere, and that the photospheric motion is unaffected by the coronal magnetic field, and therefore may be considered to be *prescribed*. It can be shown that the energy stored by ideal, line-tied, quasi-static evolution will always exceed the energy of the corresponding FCE (Longcope 2001). This means that the MCC may be used to provide a lower bound on the energy stored by ideal quasi-static evolution under line-tied evolution. Moreover, all the free energy

[1]It has been argued that (see Longcope & van Ballegooijen 2002), at least for the smallest photospheric flux concentrations, an assumption of perfect line-tying is no more physically plausible than the assumptions of MCC.

of the MCC may be released by making only topological changes to field lines in the vicinity of the current sheet; i.e. by reconnection. This feature of the model follows simply from the fact that FCEs are minima subject to constraints, and that these constraints are violated (i.e. eliminated) by a field-aligned electric field at a separator. In this manner it is possible for local topological changes of a few field lines to release energy which is stored globally throughout the coronal volume. The MCC thereby provides a self-consistent model of energy release by magnetic reconnection in three-dimensional fields of arbitrary complexity.

For all of the above reasons the MCC is a powerful tool for modeling realistic coronal magnetic fields. Provided that observed photospheric fields may be approximated as discrete sources, the MCC permits ready calculation of a lower bound on the free magnetic energy stored by ideal coronal evolution driven by observed photospheric evolution. It also provides a lower bound on the energy liberated by reconnection at a small number of topologically significant locations: the separators.

While the MCC is self-consistent given its assumptions, it is not consistent with arbitrary line-tied photospheric motions. Photospheric line tying is commonly used in MHD simulations, so the MCC will not exactly match their results. The MCC does still provide a lower bound on their free magnetic energy (provided they have zero resistivity), and may still serve as an approximation of the simulated evolution. It is not, at present, clear how reliable an approximation the MCC is to line-tied evolution. Indeed, simulations of quasi-static coronal evolution driven by line-tied photospheric motions have shown qualitative similarities with MCC, including a tendency for large current densities to develop along the magnetic separator (Galsgaard et al. 2000). These results do not, however, quantify the accuracy of the MCC as an approximation for line-tied evolution. Nor have they led to an estimate of how much greater is the free energy of the line-tied field than that of the lower bound, the FCE.

Line-tied *resistive* simulations differ from both of the ideal cases in still other respects. First of all, since resistive simulations are necessarily dynamic, their energetics will depend on the *rate* of photospheric driving, in contrast to quasi-static models. As outlined above, ideal line-tied simulations accumulate currents both distributed within domains and concentrated at domain interfaces. In the presence of resistivity both types of current will diffuse, with the more concentrated interface currents diffusing most quickly. Their ultimate magnitude will be determined by the balance between the rate of photospheric driving and the rate of resisitve dissipation. Dissipation on even Sweet-Parker time scale would render the interface currents relatively weak even when the system's magnetic Reynolds number is many thousand. The relative significance of interface currents at still higher values will depend on how each of the competing rates, current concentration and magnetic reconnection, scales

with Reynolds number. Before considering this dynamical problem, however, it is useful to consider the quasi-static limit which is necessarily non-resistive.

This work presents a comparison of quasi-static coronal evolution according to the MCC with that driven by line-tied photospheric motion in numerical simulation. The next section presents the problem which will be solved using each model. Section 3 briefly reviews the MCC and applies it to the problem. Section 4 describes the numerical simulation and presents its results. Section 5 makes a comparison of the two, and explains the differences in terms of the different motions of the photospheric footpoints in the two models. This difference is quantified in terms of relative helicity injection. Finally, section 6 discusses the implications of these results for understanding the quasi-static evolution of an arbitrary coronal magnetic field.

2. The problem

We will study a magnetic configuration which is sufficiently complex that it contains a separator. The simplest such configuration is an arrangement of four photospheric sources, i.e. a general quadrupole (Sweet 1958b; Baum & Bratenahl 1980; Longcope 1996; Longcope & Klapper 2002).[2] We consider a family of such configurations in which each source is a disk of radius a containing flux $\pm\Phi_0$ symmetrically distributed as vertical field B_z, whose radius of gyration is $\bar{a}$:

$$\bar{a}^2 \equiv \frac{2\pi}{\Phi_0}\int_0^a |B_z(r)| r^3\, dr \;\leq\; a^2 \quad .$$

This configuration conforms exactly to the discrete-source assumption of the MCC. The sources compose two dipoles, each centered at the origin, whose axes are mis-aligned with one another by angle θ (see fig. 1). The separation between outer poles is $2d$, while the inner bipole is smaller by a factor $\epsilon < 1$. We further assume the simplest coronal field topology consisting of four *flux domains*, whereby each source is connected to both opposing sources. There is therefore a single magnetic separator lying in the middle of the four domains.

[2]The same topology is possible for three sources whose net flux is not zero. In this case infinity functions as a fourth "source" of flux.

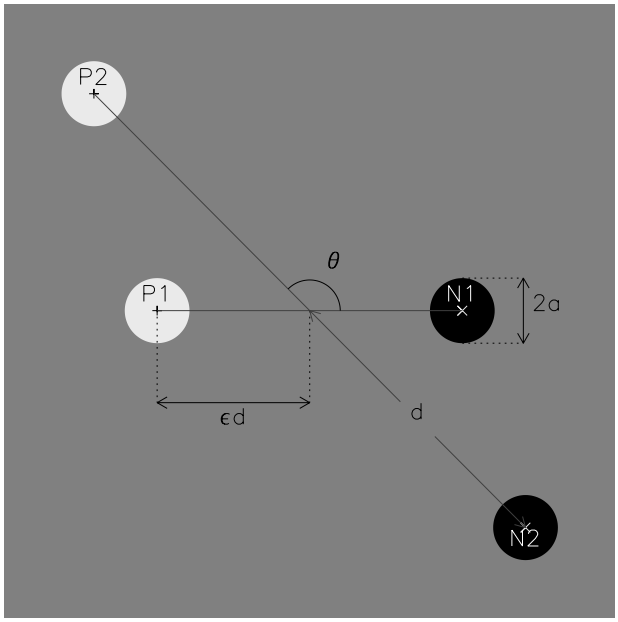

Fig. 1.— The generalized quadrupole consisting of four photospheric sources, $P1$, $P2$, $N1$ and $N2$. Each source is a disk of radius a and flux $\pm\Phi_0$. The outer and inner dipoles have separations $2d$ and $2d\epsilon$ respectively. The axes of the dipoles make an angle θ with respect to one another.

Our present investigation will follow the slow, dynamical evolution of the coronal magnetic field as the photospheric field progresses through a sequence of angles θ, beginning at $\theta_0 = \pi/4$. The initial condition for this evolution will be a potential coronal field ($\nabla \times \mathbf{B} = 0$). The outer sources, $P2$ and $N2$ will remain fixed while the inner bipole rotates about the origin. We will further restrict consideration to an inner bipole parameter $\epsilon = 0.283$. The radius of the source regions, a, will be fixed during the evolution, however, we will have occasion to consider several values including $a = 0$ for which the source regions are magnetic point-charges. We characterize the photospheric evolution only by the motions of entire source regions and *not* by the footpoint motions *within* a region; the two subsequent sections differ principally in the internal motions they assume.

The initial (potential) magnetic field contains two null points, $A1$ and $B2$, both located on the source plane, $z = 0$. The fan surfaces from these two null points form separatrix surfaces which together divide the coronal volume into its four flux domains (Longcope & Klapper 2002), designated by the source regions at each footpoint $P1$–$N1$, $P1$–$N2$ and so on. The separatrices in this potential field intersect along a single curve, the separator field line, which begins at $B2$ and ends at $A1$ (see fig. 2b). Adding a return path along the field-free portion of the photosphere forms a closed curve $\mathcal{Q}$ enclosing all those field lines connecting $P1$ to $N1$.[3] The flux enclosed by $\mathcal{Q}$, called $\Psi^{(\mathrm{v})}(\theta_0)$, is the flux of domain $P1$–$N1$ in the initial field, which is a "vacuum" or potential magnetic field. For the case of point sources ($a = 0$) this is $\Psi^{(\mathrm{v})} = 0.455\Phi_0$, and we show below that this value changes little for finite, uniform disks. This means that of the total flux Φ_0 leaving sources $P1$, 45.5% connects to $N1$ and 54.5% to $N2$.

[3]See Longcope & Klapper (2002) for a more detailed discussion of this calculational procedure.

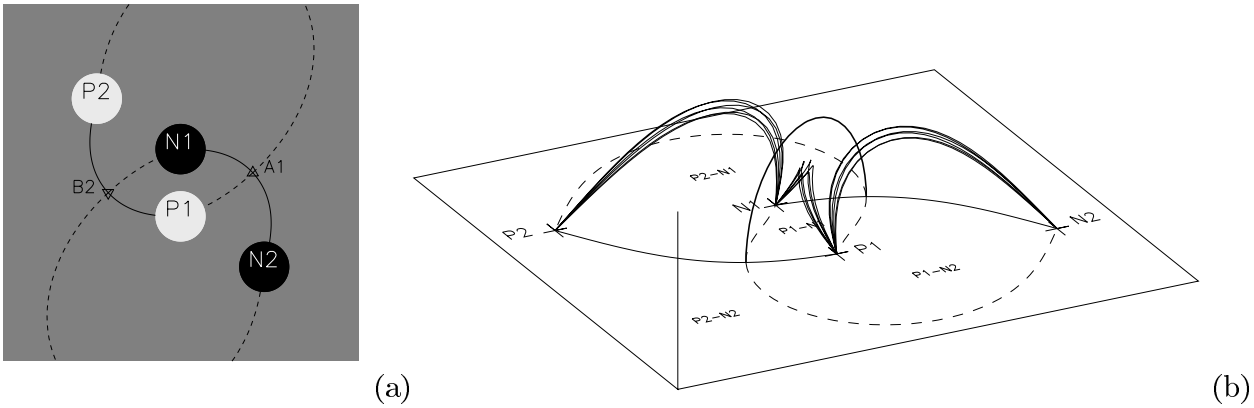

(a) (b)

Fig. 2.— The initial coronal magnetic field. (a) The photospheric source regions with radius of gyration $\bar{a} = 0.375\epsilon d$. Null points $A1$ and $B2$ are shown (triangles) along with their spines (solid) and photospheric footprints of their separatrices (dashed). (b) Projection view of the point-sources case ($a = 0$). Field lines from three domains are shown along with the separator.

Our goal is to characterize the coronal-field evolution as the photospheric sources move in the manner described above. To capture the character of the actual solar corona in a simplified model we take the coronal plasma to be perfectly conducting[4] and to have vanishingly small pressure ($\beta \to 0$). We also consider the photospheric motion to be slow relative to coronal Alfvén times, $d\theta/dt \ll v_{\rm A}/d$. Under these conditions we expect the corona to evolve through a sequence of magnetic equilibria characterized by the bipole-alignment angle θ.

3. The Minimum Current Corona

According to both the MCC and line-tied, ideal MHD, the net fluxes in each of the four flux domains will remain constant during evolution. Having established the flux of one domain, say $\psi_{11} = 0.455\Phi_0$ in domain $P1$–$N1$, the values of the other three follow immediately from the net source fluxes (Longcope 2001). For example $\psi_{12} = \Phi_0 - \psi_{11}$ since any flux leaving $P1$ which does not connect to $N1$ must connect instead to $N2$. This means that the MCC evolution proceeds through equilibria for which the flux in domain $P1$–$N1$ is fixed at $\psi_{11} = \Psi^{(\rm v)}(\theta_0)$.

Calculating the domain fluxes in every potential field yields the function $\Psi^{(\rm v)}(\theta) = \psi_{11}$, the flux linked by the separator path $\mathcal{Q}$ in the vacuum (potential) field. Figure 3 shows $\Psi^{(\rm v)}(\theta)$ for the case of point sources, $a = 0$, and uniform disks whose radii of gyration are $\bar{a} = 0.375\epsilon d$. As θ increases $\Psi^{(\rm v)}$ increases as well, as a natural consequence of the growing separation between $P1$ and $N2$ making the alternate connection, $P1$–$N1$, increasingly "favorable".

[4]The actual corona has a finite conductivity which is very large in the corona, and decreases in cooler atmospheric layers. The magnetic Reynold's number is sufficiently large, $Rm \sim 10^{10}$, that the assumption of zero resitivity is frequently made.

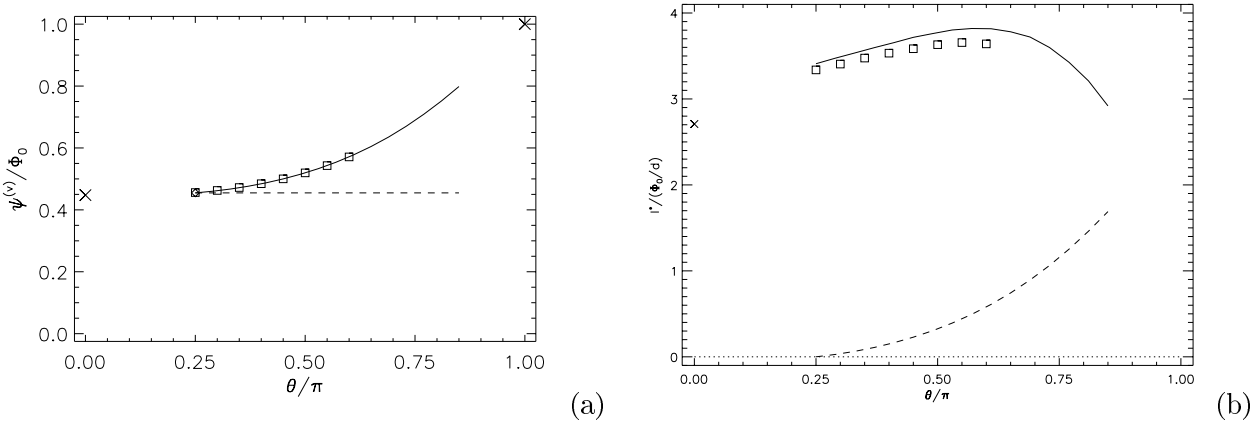

Fig. 3.— Characteristics of the potential fields as a function of mis-alignment angle θ for point sources ($a = 0$ solid line) and disks ($\bar{a} = 0.375\epsilon d$, squares). The axisymmetric cases of co-linear points, $a = 0$ and $\theta = 0$ or π, are shown with $\times$s. (a) shows the flux $\Psi^{(\mathrm{v})}$ in domain $P1$–$N1$, normalized to Φ_0. The dashed line is the value $\Psi^{(\mathrm{v})}(\theta_0)$. (b) shows the characteristic current $I^\star$ normalized to Φ_0/d. The dashed curve is $4\pi|\Delta\Psi|/L$.

The flux constrained equilibrium (FCE) will be a potential field only when the prescribed flux inside separator loop $\mathcal{Q}$, designated Ψ, matches that of the potential field $\Psi^{(\mathrm{v})}(\theta)$. In cases where it does not match, the equilibrium field will be current-free except for a current ribbon forming the separator. This fact follows from the Euler-Lagrange equations resulting from the energy minimization (Longcope 2001), although there few cases in which these equations may be actually solved.

It is possible to estimate the properties of the current ribbon in cases where the flux difference $\Delta\Psi \equiv \Psi - \Psi^{(\mathrm{v})}$ is sufficiently small (Longcope 1996, and Appendix). Under this assumption the current follows a path approximating the separator of the potential field, and affects the field only in its immediate neighborhood. Furthermore, the width of the current ribbon, Δ, is set by the current I and the potential field in the immediate vicinity of the separator. The self-flux produced by this current ribbon can be written

$$\Psi^{(\mathrm{cr})} \;=\; \frac{IL}{4\pi}\,\ln(eI^\star/|I|) \tag{1}$$

where L is the length of the potential-field separator, $e = 2.718$ is the base of the natural logarithm. The current $I^\star$ is a quantity, defined precisely in an Appendix, proportional the average perpendicular magnetic shear along the potential-field separator.[5] We show below that a current sheet carrying $|I| = I^\star$ will extend a width Δ comparable to the diameter of the loop.

The flux constraint requires that $\Psi = \Psi^{(\mathrm{v})} + \Psi^{(\mathrm{cr})}$ from which we may solve for the net current in the ribbon

$$I \;=\; I^\star\,\Lambda^{-1}(4\pi\Delta\Psi/LI^\star) \quad , \tag{2}$$

where the function $\Lambda(x) \equiv x\ln(e/|x|)$ is invertible provided $|\Lambda| \le 1$; we will assign its inverse the unique value from the range $|x| \le 1$. Currents outside this range, $|I| \ge I^\star$, behave in the unphysical manner characteristic of a negative self-inductance: additional current *decreases* the self-flux.

Equation (1) is only strictly valid when $|I| \ll I^\star$, however, when tests are possible they often show it to apply over a wider range (Longcope 2001; Longcope & van Ballegooijen 2002). The present configuration may be subjected to such a test by considering the particular case $a = 0$ and $\theta = 0$ which is an axisymmetric field from co-linear point sources. Due to the axisymmetry the potential-field separator is a semi-circle of X-points enclosing a flux $\Psi^{(\mathrm{v})} = 0.448\Phi_0$ and with a magnetic-shear parameter $I^\star = 2.71\Phi_0/d$ (both the values

[5]We use rationalized electro-magnetic units where $\nabla\times\mathbf{B} = \mathbf{J}$ and thus $I \equiv \oint \mathbf{B}\cdot d\mathbf{l}$. Expressions may be converted to MKS or cgs-esu by replacing I with $\mu_0 I$ or $4\pi I/c$ respectively.

are denoted by crosses in fig. 3). An equilibrium with $\Psi \neq \Psi^{(\mathrm{v})}$ has a current sheet located where the ring of X-points appeared in the potential field.

We expect the largest currents in the limiting cases where $P1$ and $N1$ share no flux, $\Psi = 0$, or where they share all their flux $\Psi = \Phi_0$. The field for each case has the same structure, but different direction, as a potential field where the signs of certain sources has been reversed ($N1$ and $P2$ are reversed in the first case, $P1$ and $N1$ in the second). The net current for the equilibrium current sheet is calculated as $\int \mathbf{B} \cdot d\mathbf{l}$ in this "sign-reversed" field, along the surface which becomes a current sheet when the directions of field lines from reversed sources are restored (see Zhang & Low 2001, for more detailed examples of this technique). The first limiting case has an infinite current sheet on the plane bisecting $P1$ and $N1$, whose net azimuthal current is $I = -2(\epsilon^{-1} - 1)(\Phi_0/d)/\pi$. In the second case the current sheet forms a closed surface enveloping $P1$ and $N1$. Remarkably, both limiting currents fall very close to the analytic approximation given by (1) as shown in fig. 4. This is just one example of how the approximate current-flux relation appears to be useful over a wider range of currents than its derivation can justify. We will henceforth adopt relationship (2) to predict the separator current during quasi-static evolution.

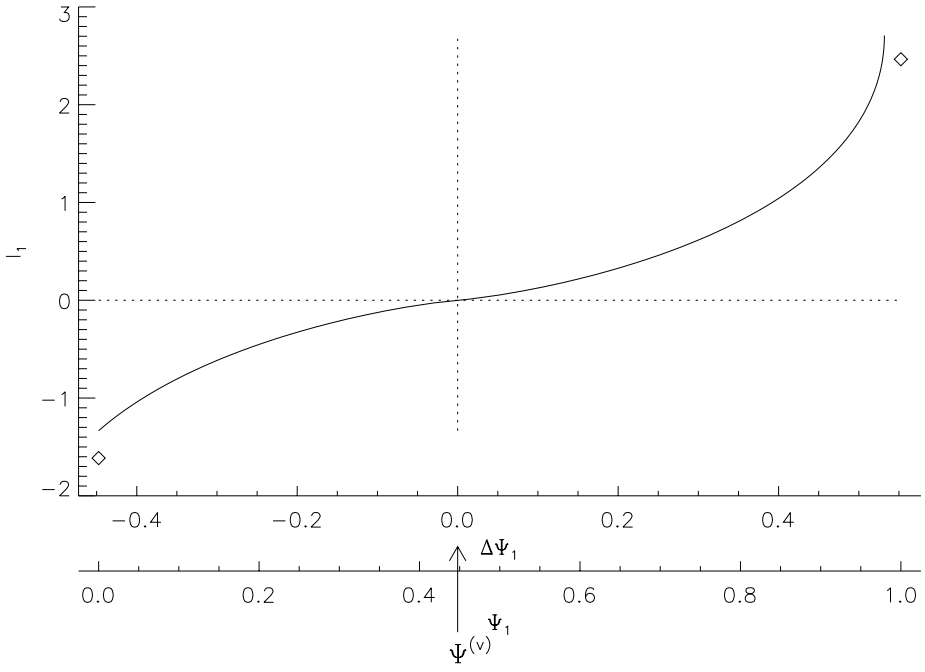

Fig. 4.— Currents in the flux-constrained equilibrium for the axisymmetric field $a = 0$, $\theta = 0$. The current I (solid, normalized to Φ_0/d) from approximate expression (2) are plotted versus $\Delta\Psi$ (upper axis) and Ψ (lower axis), both normalized top Φ_0. The potential field occurs when $\Psi = \Psi^{(v)} = 0.448\Phi_0$, indicated by an arrow. Diamonds indicate the analytic results for the two limiting cases $\Psi = 0$ and $\Psi = \Phi_0$.

The small-current approximation can also be used to predict the width of the current sheet Δ in terms of a local magnetic shear parameter B' (see Appendix). Approximating the vicinity of the separator by a two-dimensional current sheet gives

$$\Delta \;=\; \sqrt{\frac{4|I|}{\pi B'}} \;=\; \frac{L}{\pi}\, 32 e^{-2} \sqrt{s \frac{|I| \bar{B}'}{I^\star B'}} \quad , \tag{3}$$

where $\bar{B}'$ is the geometric mean of the perpendicular magnetic shear and s parameterizes the non-circularity of the vacuum separator; it is typically found to be close to unity (see Appendix). Unlike the flux-current relationship, this cannot be applied to currents $|I| \sim I^\star$, since it would predict a width larger than the pseudo-radius of the loop, L/π. In the case of axisymmetry $\bar{B}' = B'$ and $s = 1$. In the disconnected axisymmetric case, where $I = -1.6 I^\star$, the current sheet extends inward to the axis and outward to infinity; a result not well approximated by (3).

Applying the analytic expression (2) to the evolution from $\theta_0 = \pi/4$ onward gives the current $I(\theta)$ shown in fig. 5. This shows the current carried by the separator ribbon increases as θ increases. The current is negative since it flows counter to the direction of the separator field line, which always goes from the positive null to negative null ($B2 \rightarrow A1$ for this separator). This is the direction predicted by Lenz's law, in order to counter-act the increase in $\Psi^{(\mathrm{v})}$, and thereby keep the domain flux ψ_{11} fixed.

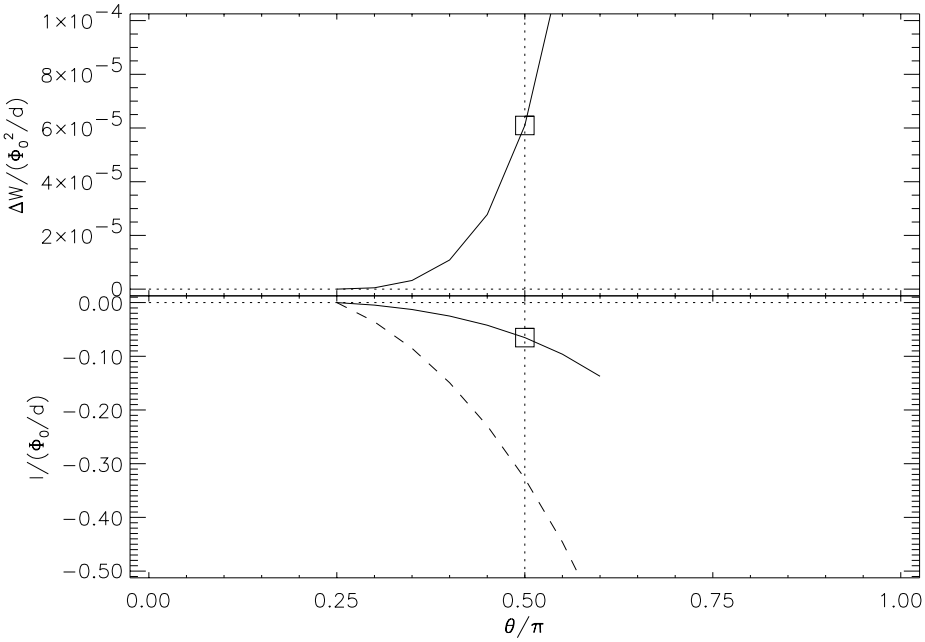

Fig. 5.— The values of separator current I (solid curve, bottom panel) and free magnetic energy ΔW (solid curve, upper panel) versus the mis-alignment angle θ. For reference the dashed curve shows $4\pi\Delta\Psi/L$, also shown in fig. 3b.

The free energy in the entire magnetic field can be calculated by integrating the electromagnetic work required to change the flux inside the current sheet from $\Psi^{(\mathrm{v})} \rightarrow \Psi$. Using expression (1) we find (Longcope 2001)

$$\Delta W_{\mathrm{MCC}} \;=\; \frac{1}{4\pi}\int_{\Psi^{(\mathrm{v})}}^{\Psi} I\, d\Psi \;=\; \frac{LI^2}{32\pi^2}\ln\left(\frac{\sqrt{e}I^\star}{|I|}\right) \quad . \tag{4}$$

This is the magnetic energy in excess of the potential field, and it can be seen in (4) that ΔW_{MCC} vanishes as $I \rightarrow 0$. In fig. 5 the free energy is plotted against θ beginning with a potential field at $\theta = \pi/4$. The free energy can, in principle, be liberated by eliminating, through reconnection across the separator, the constraint that ψ_{11} maintain a fixed value.

The MCC therefore predicts a current sheet carrying current I, flowing in a sheet along the separator. Using the approximate width from expression (3), and following the separator field line from the potential field gives the configuration shown in fig. 6. Figure 6b shows the view within a sectioning plane $x = 0$. In the potential field, the separatrices, Σ_A and Σ_B (dashed) cross at the separator (diamond). This resembles the classic X-point configuration found in two-dimensional models. As in two-dimensional models (Green 1965; Syrovatskii 1971) stress on the field causes the X-point to develop into a current sheet, shown here as a vertical line. The sheet has significant extent even for the rather small separator current of $I = -0.017I^\star$ found from (2). A perspective view of the full current sheet is shown in fig. 6a.

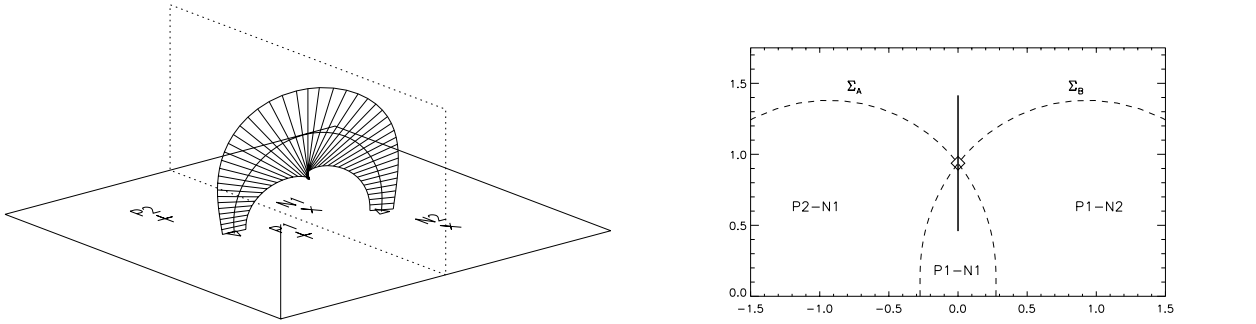

(a) (b)

Fig. 6.— The current ribbon predicted by MCC for the angle $\theta = \pi/2$. (a) A perspective view of the predicted current ribbon. A dotted box shows the sectioning plane $x = 0$. (b) The flux domains within the sectioning plane. Dashed curves are the separatrices of the potential magnetic field, Σ_A and Σ_B, which intersect at the separator (diamond). The bold solid line is the approximate current sheet extent for $I = -0.064(\Phi_0/d) = -0.017I^\star$.

4. The numerical simulation

4.1. Basic equations and simulation domain

The objective of this work is to compare the MCC to a numerical solution of ideal, quasi-static, line-tied evolution. To do this we solve the equations of time-dependent, compressible, ideal MHD without gravity for a three-dimensional half-space above a line-tied photospheric boundary. The equations solved are

$$\frac{\partial \rho}{\partial t} + \nabla \cdot (\rho \mathbf{v}) = 0, \tag{5}$$

$$\rho \left[\frac{\partial \mathbf{v}}{\partial t} + (\mathbf{v} \cdot \nabla) \mathbf{v} \right] = -\nabla P + \frac{1}{4\pi} (\nabla \times \mathbf{B}) \times \mathbf{B}, \tag{6}$$

$$\frac{\partial}{\partial t} \left(\frac{P}{\rho^\gamma} \right) + \mathbf{v} \cdot \nabla \left(\frac{P}{\rho^\gamma} \right) = 0, \tag{7}$$

$$\frac{\partial \mathbf{B}}{\partial t} = \nabla \times (\mathbf{v} \times \mathbf{B}), \tag{8}$$

where ρ, $\mathbf{v}$, $\mathbf{B}$, P, and γ are the mass density, fluid velocity, magnetic field, plasma pressure, and adiabatic index, respectively (the monatomic value $\gamma = 5/3$ is used).

Equations (5) – (8) are solved in Cartesian coordinates where x and y are horizontal and z is vertical, increasing upward, within a rectangular domain $(-3.53, -3.53, 0) \leq (x, y, z) \leq (3.53, 3.53, 5.30)$ in units of d, the half-separation between the outermost poles. The domain is filled with a non-uniform $173 \times 173 \times 98$ Cartesian-product grid whose spacing is smallest, $(\Delta x, \Delta y, \Delta z) = (0.0177, 0.0177, 0.0177)$, within a central region $|x|, |y|, |z| \leq 0.707$, and increases to to $(0.141, 0.141, 0.177)$ at the outer edges of the box. The unknowns are time-advanced using a modified Lax-Wendroff numerical scheme (see Magara 1998, for details)

At the photospheric boundary ($z = 0$), the horizontal velocity is specified by a time-dependent function given below and the vertical velocity is always zero. The gas pressure and gas density at this boundary retain their initial value, while the vertical magnetic field is obtained by advection according to the prescribed horizontal velocity field. The horizontal magnetic fields at the photospheric boundary are updated by solving the induction equation, using a layer of ghost points located at $z = -\Delta z$ which are given the same velocity and magnetic field as the photospheric boundary. We impose a stress-free boundary condition at the other boundaries (top and sides), according to which all the physical quantities are calculated via zeroth order extrapolation except for velocity which is set to zero. We also place wave-damping areas near all the boundaries but the bottom one (Magara 1998).

4.2. Lower Boundary and Initial Conditions

The vertical field prescribed at the lower boundary consists of four isolated sources each of radius $a = 0.212d$. Within source i, centered at (x_i, y_i),

$$B_z\left(r_\perp\right) = \pm B_0\left(1 - \frac{r_\perp^2}{a^2}\right)^2 \quad , \quad r_\perp < a \tag{9}$$

where $r_\perp = \left[\left(x - x_i\right)^2 + \left(y - y_i\right)^2\right]^{1/2}$ is the distance from its center. Setting $\Phi_0 = \pi a^2 B_0/3$ to unity fixes $B_0 = 21.26$. The four sources are initially arranged as fig. 2a shows. The radius of gyration of each sources is $\bar{a} = a/2 = 0.375\epsilon$, the same value used in the previous section (matching the net flux and radius of gyration assures that the potential field from each source agrees with those in the MCC up to the quadrupole term). Initially the bipoles are mis-aligned with an angle $\theta_0 = \pi/4$, and the overlying corona is a potential field.

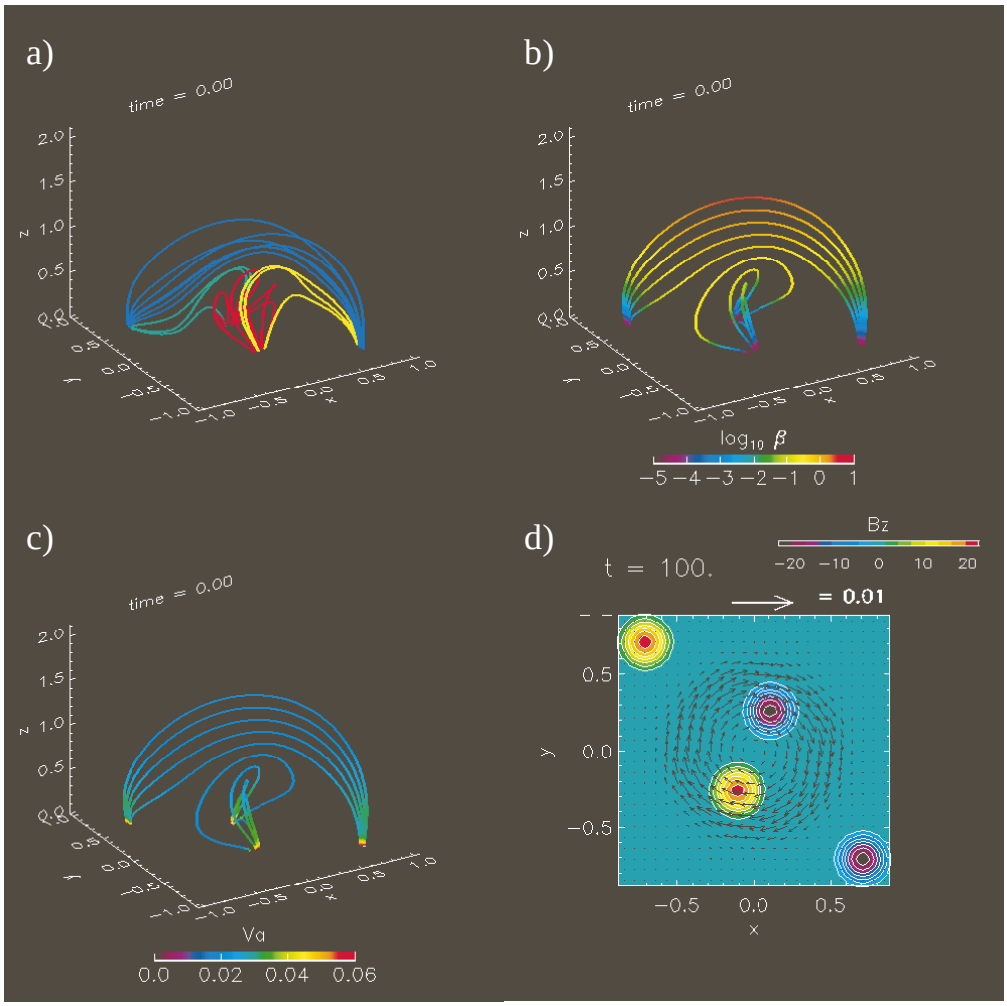

Fig. 7.— (a) Initial state of the simulation. The initial condition, consisting of a potential field above four photospheric magnetic sources. Representative field lines are shown from each of the four coronal domains: P1–N1 (red), P1–N2 (yellow), P2–N1 (green), and P2–N2 (blue). (b) Color scale shows the distribution of plasma β on each of these initial field lines. (c) The color code shows the distribution of the Alfvén velocity on the field lines of the initial field. (d) A snapshot of the imposed velocity field (arrows) and vertical magnetic flux (contours and color scales) at the photosphere, taken at $t = 100$.

The gas pressure is initially uniform $p_0 = 1.5 \times 10^{-4}$, which is sufficiently small that regions of strong field, such as the source region interiors, have $\beta = 8.4 \times 10^{-6}$ (see the plasma β distribution in 7b). In order to avoid such numerical problems as negative pressure and extremely large wave speeds, which can occur in explicit schemes, we impose absolute lower limits on both gas pressure and gas density

$$p_{\min} = 1.5 \times 10^{-5}, \tag{10}$$

and

$$\rho_{\min} = 7.1 \times 10^{-4}. \tag{11}$$

These values are close enough to the initial values, that the resulting thermodynamic evolution cannot be considered realistic. Nevertheless, due to the very low values of β the dynamical evolution of the magnetic field, which is after all the primary aim of our study, is reliable in this simulation.

Absent gravity and thermal conduction the initial density profile may be chosen without regard to pressure. For numerical convenience we choose the density to provide Alfvén velocities and sound speeds within reasonable ranges. We choose the form

$$\rho = \rho_0 \left(\frac{|\mathbf{B}|}{B_0} \right)^{\delta}, \tag{12}$$

where $\rho_0 = 3.39 \times 10^3$ and the exponent δ varies in space between 0 along the photospheric surface, and 1.6 high above. The specific form we choose to accomplish this variation is

$$\delta = 1.6 \tanh \left[\left(\frac{4\sqrt{x^2 + y^2}}{x^2 + y^2 + w^2} + \frac{1}{w} \right) z \right] \quad , \tag{13}$$

where $w = 0.353$. According to this prescription the gas density is uniformly distributed at the photosphere ($z = 0$) and correlated with magnetic field strength high in the corona. The maximum Alfvén velocity in the initial field is $v_{\rm A} = 0.059$ just above the photospheric sources (see the Alfvén velocity distribution in fig. 7c).

4.3. Imposed velocity field

The system evolves in response to the photospheric motions described in section 2: the two inner sources, P1 and N1, rotate about the origin while sources P2 and N2 remain fixed. We accomplish this motion by imposing a photospheric velocity field in which v_ϕ is a function of $r_\perp = \sqrt{x^2 + y^2}$ and t

$$v_\phi \left(r_\perp, t \right) = \frac{\pi \Delta\theta r_\perp}{4 \ t_{\rm f}} \sin \left(\pi \frac{t}{t_{\rm f}} \right) \left\{ \tanh \left[14.1 \left(r_\perp - r_0 \right) \right] - 1 \right\} \quad . \tag{14}$$

Here $r_0 = 0.566d$ is the approximate extent of the rigid rotation region, $\Delta\theta = \pi/4$ is the net angle rotated (see fig. 1, $\theta : \pi/4 \rightarrow \pi/2$), and $t_{\rm f} = 200$ is the duration of rotation. The imposed velocity starts increasing from zero at $t = 0$ and reaches the maximum, about 4% of the maximum Alfvén velocity at $t = 100$, then it starts decreasing and finally returns to zero at $t = 200$. The snapshot of the imposed velocity field taken at $t = 100$ is shown in figure 8d.

The goal of the simulation is to approximate quasi-static magnetic evolution under the ideal induction equation (8). In order to keep the system close to equilibrium we perform two intermediate operations following each velocity advance which serve to smooth and damp the velocity field. The first operation damps the motion with an artificial friction by decrementing all velocities according to the recipe

$$\mathbf{v} \;\rightarrow\; (1-\alpha)\mathbf{v} \quad , \tag{15}$$

where $\alpha = 0.1\Delta t$ is a small number. Next, the velocity at each grid point (i, j, k) is smoothed by averaging according to the recipe

$$\begin{aligned} \mathbf{v}\,(i,j,k) \;\rightarrow\; & \sigma\mathbf{v}\,(i,j,k) + \tfrac{1-\sigma}{6}\left[\mathbf{v}\,(i+1,j,k) + \mathbf{v}\,(i-1,j,k) + \mathbf{v}\,(i,j+1,k)\right. \\ & \left. +\mathbf{v}\,(i,j-1,k) + \mathbf{v}\,(i,j,k+1) + \mathbf{v}\,(i,j,k-1)\right] \end{aligned} \tag{16}$$

where $\sigma = 0.9$.

4.4. Numerical results

The resulting evolution of the four magnetic domains is shown in fig. 8. The central domain P1–N1 (red field lines) appears to rotate rigidly in accordance with expectation. The two side domains P1–N2 and P2–N1 (green and yellow field lines) are slowly deformed by the relative motions of their footpoints — their inner footpoints move while their outer footpoints remain fixed. The overlying domain P2–N2 (blue field lines), whose footpoints remain fixed, shows no significant change.

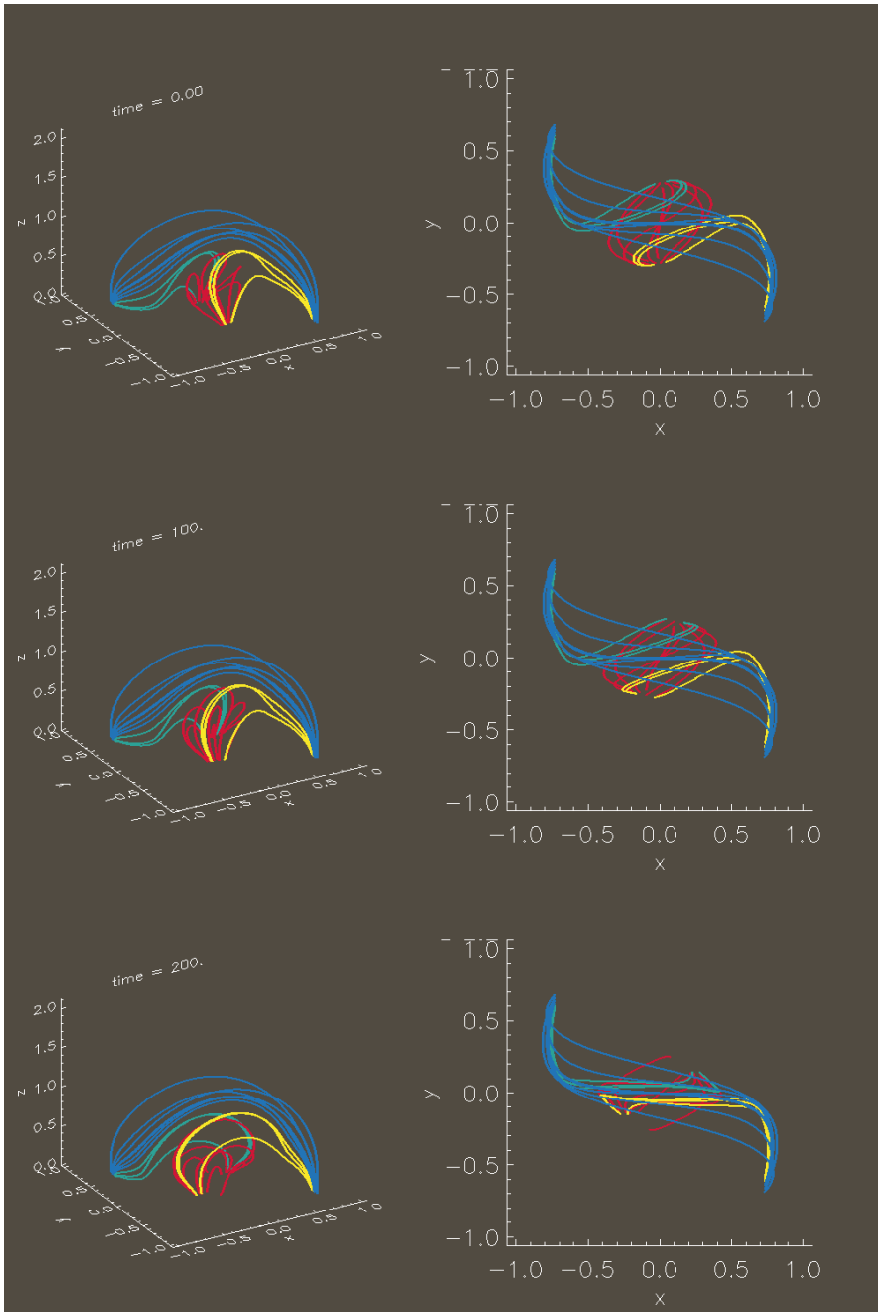

Fig. 8.— Temporal development of flux domains: $t = 0$ (upper panel), $t = 100$ (middle panel), and $t = 200$ (lower panel).

The relative motions of these domain creates a distribution of current density concentrated along the interfaces, as shown in fig. 9. In order to de-emphasize transient currents, we plot field-aligned current density, $J_s \equiv \mathbf{J} \cdot \mathbf{B}/\left|\mathbf{B}\right|$, where it crosses the sectioning plane $x = 0$. In each panel, field lines that belong to the central and overlying domains are shown in blue. Since the central domain, $P1$–$N1$, rotates relative to the overlying domain, $P2$–$N2$, a current is generated at the boundary separating those domains. The development of this current, called *inter-domain current*, can be observed as a growing spot near the z axis on the sectioning plane which begins orange and later turns blue. This region of highest current density forms a vertical strip in the later phase ($t = 200$). Additional current-concentration occurs inside the two side domains and inside the central domain, which appear as green regions by $t = 200$. Field lines in the side domains, $P1$–$N2$ and $P2$–$N1$, are subjected to relative motions of their footpoints leading to current inside the domain, called *intra-domain current*. These domains also change shape with time, which eventually compresses central domain causing at least temporally, intra-domain current in $P1$–$N1$ even though this domain rotates rigidly, and therefore has no relative internal footpoints motions imposed.

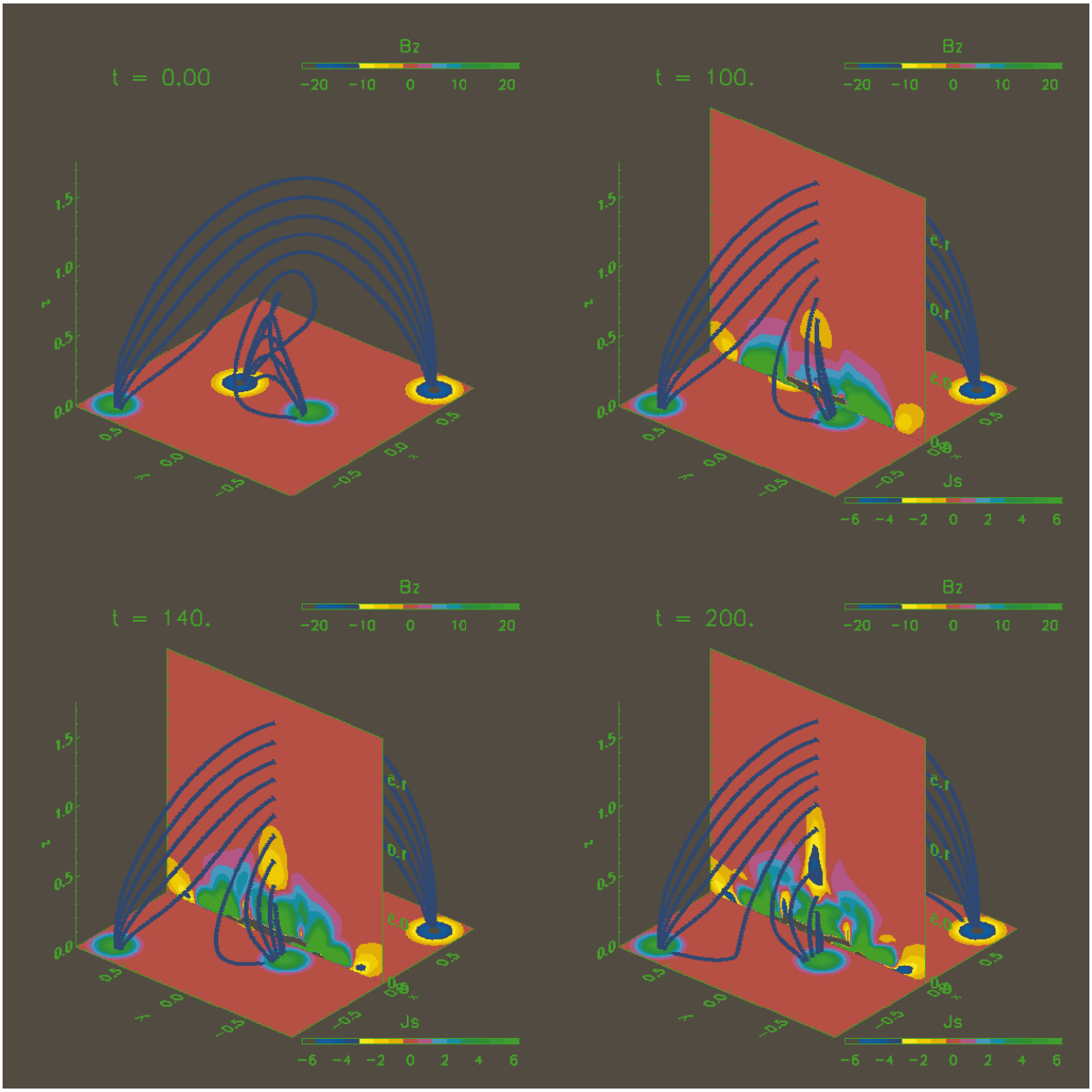

Fig. 9.— Time history of field-aligned current on the sectioning plane at $x = 0$. A color map on the bottom plane shows the distribution of vertical magnetic field. Only the field lines belonging to the central domain and overlying domain are shown by blue lines.

5. Comparison

To interpret the simulation results in terms of the MCC model we plot the local field line twist parameter $\alpha \equiv J_s/|\mathbf{B}|$ within the sectioning plane (fig. 10). This shows clearly the negative concentration of field-aligned current (dark) along the interfaces of the flux domains. The intra-domain current appears in regions of strong field and is not as evident in the plot of $\alpha(y, z)$. For comparison we overlay the features of fig. 6b showing the separatrices of the potential field (dotted) and the extent of current sheet predicted by expression (3). The current sheet is thus an extrapolation to large currents of an approximation valid for infinitesimal currents which, as discussed in sec. 3, is never as accurate as the net current; it is shown primarily as a visual guide. The dashed lines are meant to indicate the modified shape of the separatrices expected in the FCE; they are constructed by connecting the tips of the predicted current sheet to the bottoms of the potential-field separatrices. The central concentration of α (dark) conforms to this predicted shape, showing a vertical current sheet located approximately where the potential field's separator had been.

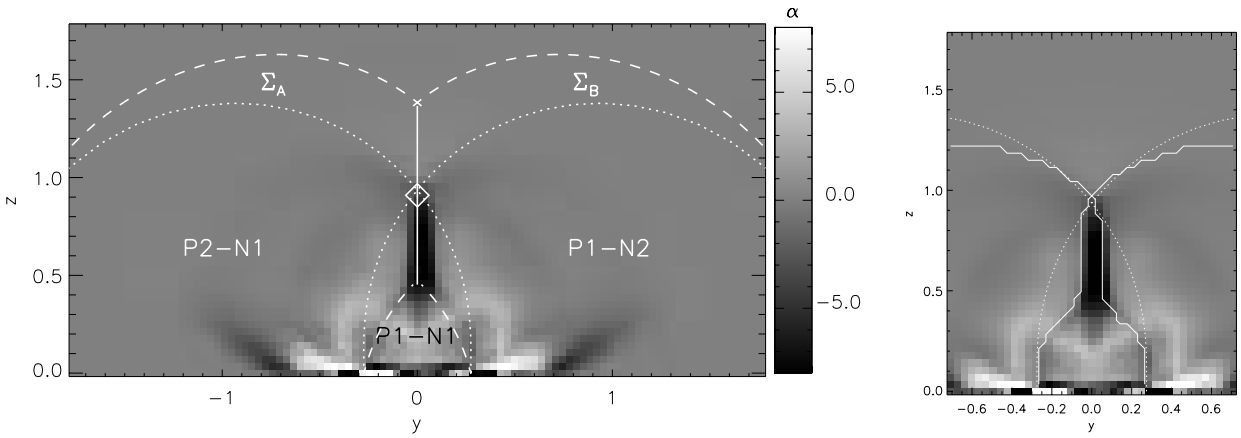

Fig. 10.— A grey-scale plot of the twist parameter $\alpha(y, z) = J_s/|\mathbf{B}|$ within the sectioning plane $x = 0$ from the final time of the simulation, $t = 200$. Dotted lines show the separatrix of the potential field. Left panel: The solid vertical line shows the predicted extent of the current sheet (solid) and dashed lines indicate expected shape of separatrix in the flux-constrained equilibrium. Right panel: The location of the actual separatrix at $t = 200$.

The right panel of fig. 10 shows the actual separatrices found by tracing field lines from a grid of points in the sectioning plane to one of the distinct photospheric sources. The two curves cross at that point the separator pierces the sectioning plane. It is noteworthy that the separator in the actual field is located very near where it would be in a potential field. Below the separator the separatrices have converged relative to those in the potential field, as a result of the current sheet. Above the separator the separatrices are much closer to those of the potential field. Finally, there are two dark, diagonal bands emanating from $y \simeq \pm 0.7$ at the photosphere. The diagonal bands are seen below to be related to the edge of the rigid rotation region at a radius $r = r_0 = 0.566$.

A horizontal slice made slightly above the photosphere ($z = 0.07$), shown in fig. 11, reveals that the ribbons of large negative α remain near the separator. The separatrices in this slice are also very similar to those of the potential magnetic field, departing most notably where they pinch toward the current ribbon at the separator. Two negative layers outside of parallel positive layers lie just outside the region of rigid photospheric rotation, $r = r_0 = 0.566$ (black dotted line). The negative layers intersect the sectioning plane ($x = 0$) at $y \simeq \pm 0.8$ and are clearly the top-view of the "diagonal bands" from fig. 10. (Indeed, more careful inspection of fig. 10 reveals traces of the positive layers inside the negative bands.) This suggests that these currents result from dynamical transients evolving very slowly (more slowly even than the slow footpoint motion) due to the small Alfvén speeds in the field-free portions of the photosphere. Since our objective is to study quasi-static coronal evolution we will henceforth ignore these transient features confined to the bottom of the corona.

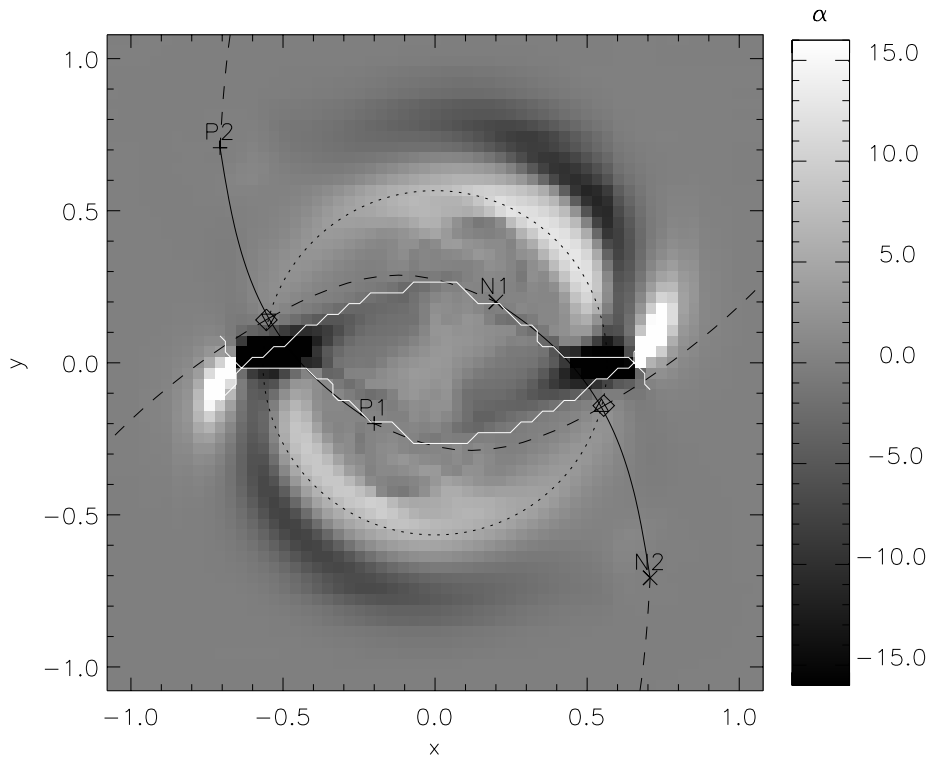

Fig. 11.— A horizontal plane just above the photosphere ($z = 0.07$) at $t = 200$. The grey-scale shows the local twist $\alpha(x, y)$. Solid and dashed black lines are the spine and fan-trace (respectively) of the separatrices at $z = 0$, exactly as in fig. 2. White solid lines are the actual separatrices of the field. The black dotted line is the circle at $r = r_0 = 0.566$ inside which the photosphere was rigidly rotated.

To make a quantitative comparison of the simulation to the MCC we define I_s as the integrated field-aligned current J_s in the inter-domain system. We first define a rectangular region, within the sectioning plane, encompassing the current sheet. We then sum J_s over all pixels where $J_s < 0$, to find I_s. Figure 12 shows the values of I_s (crosses) plotted against the rotation angle θ. The value predicted by the MCC (solid line) is less than the observed current. We describe in the following section why this may happen.

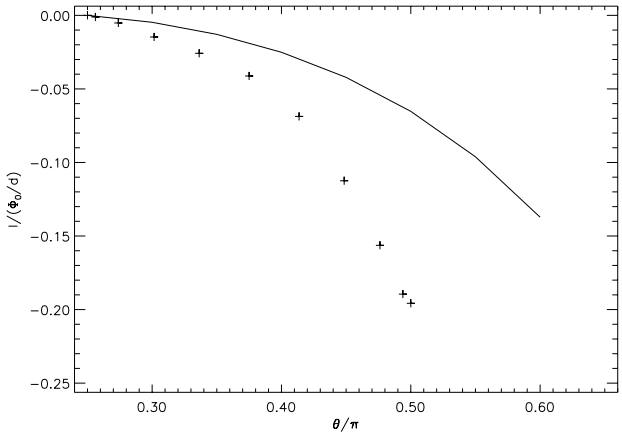

Fig. 12.— Inter-domain field aligned current I_s plotted against the angle of rotation θ. The solid line show the separator current $I(\theta)$ predicted by MCC.

5.1. The Discrepancies

In order to assess the significance of the evident differences between the simulation and the MCC, we must understand the degree to which the simulation adheres to the MCC assumptions. The photospheric flux distribution was designed to exactly conform to the discrete-source assumption, so this will not be a source of discrepancy. Conforming to FCE assumption, on the other hand, requires first that the system remain close to equilibrium (quasi-static evolution), and second that footpoints move appropriately within each photospheric source regions. We have attempted to adhere to the first part of this by moving the photosphere as slowly as possible, and further by damping excess velocity. The kinetic energy of the system remains below $2 \times 10^{-3}\,\Phi_0^2/d$, which is less than one percent of the magnetic energy. To see where the field departs most from force-free equilibrium we plot the quantity $|\mathbf{J} \times \mathbf{B}|/|\mathbf{B}|^2$. There are significant departures from force balance at the separator current sheet, where α is greatest. The ratio of these two values, $|\mathbf{J} \times \mathbf{B}|/|\mathbf{J} \cdot \mathbf{B}| \simeq 0.25$ implies that current makes a relatively small angle $\simeq 14^\circ$ with the the magnetic field in the vicinity of the current sheet. It is likely that the strong current there is out of equilibrium, and is pinching inward. The most significant distribution of Lorentz force appears to be near the photospheric sources, and the boundary of the rotating region, corroborating our previous assertion that this lowest layer harbors dynamical transients.

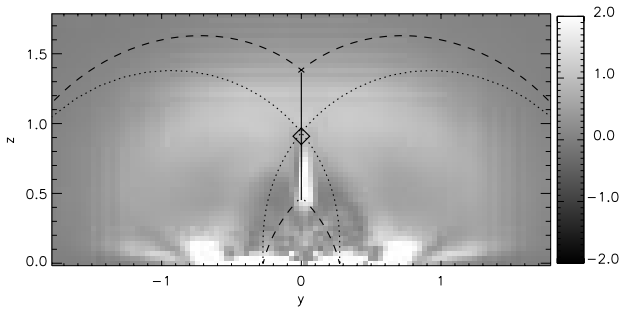

Fig. 13.— A plot of the normalized Lorentz force, $|\mathbf{J} \times \mathbf{B}|/|\mathbf{B}|^2$. This ratio of this quantity to α gives the tangent of the angle between current and magnetic field, on a scale in which grey is zero. The lines are the same as in fig. 10.

The simulation is bound to violate the FCE assumption of the MCC since it uses line-tied photospheric boundary conditions. If the simulation were performed perfectly quasi-statically, and with absolutely no resistivity, it would approach force-free magnetic fields $\mathbf{B}^{(\mathrm{LT})}$, satisfying the line tying constraints, rather than the flux-constrained equilibria $\mathbf{B}^{(\mathrm{FCE})}$ assumed by the MCC. The flux constrained equilibrium can, in principle, be approached beginning from the line-tied equilibrium through a series of additional footpoint motions. These motions should be internal to each source and should, in each case, decrease the overall magnetic energy. At any place where the current $\nabla \times \mathbf{B}^{(\mathrm{LT})}$ enters a source, it is possible to untwist those footpoints, eliminate the current and thereby decrease the field's overall energy. The Euler-Lagrange equations from the minimization (Longcope 2001) show that when minimum energy is achieved, $\mathbf{B} = \mathbf{B}^{(\mathrm{FCE})}$, no current enters any source — all domains are current-free.[6] This sequence of footpoint motions which permits the transformation $\mathbf{B}^{(\mathrm{LT})} \rightarrow \mathbf{B}^{(\mathrm{FCE})}$ demonstrates the extent to which the footpoint mappings of the two equilibria disagree.

5.2. Magnetic helicity evolution

The difference in footpoint mappings between $\mathbf{B}^{(\mathrm{LT})}$ and $\mathbf{B}^{(\mathrm{FCE})}$ is the principal source of discrepancy between the simulation and the MCC. A simple way to quantify this discrepancy is to compare the relative helicities of the two fields. The relative helicity of a magnetic field occupying the half-space $z > 0$ is (Berger & Field 1984; Finn & Antonsen 1985)

$$H_R \;=\; \int_{z>0} (\mathbf{B} - \mathbf{B}_p) \cdot (\mathbf{A} + \mathbf{A}_p)\, d\mathbf{x} \quad , \tag{17}$$

where $\mathbf{B}_p$ is a potential magnetic field matching $B_z(x, y, 0)$, and $\mathbf{A}$ and $\mathbf{A}_p$ are vector potentials for the actual and potential magnetic fields respectively. This expression for magnetic helicity has been rendered gauge-invariant by defining it relative to the helicity of the potential magnetic field $\mathbf{B}_p$. This naturally means that $H_R = 0$ when $\nabla \times \mathbf{B} = 0$ (i.e. when $\mathbf{B} = \mathbf{B}_p$).

Magnetic helicity provides a measure of how much, on average, the field-lines in an equilibrium twist about one another. Helicity is locally conserved under ideal evolution, in which case its change depends on a flux due to footpoint velocities $\mathbf{v}(x, y)$, and not on the

[6]It also implies that there are no currents on separatrices, since all separatrix field lines, except separators, have one footpoint in a source.

coronal field, (Berger & Field 1984)

$$\frac{dH_R}{dt} = -2\int_{z=0} (\mathbf{A}_p \cdot \mathbf{v}) B_z \, dx \, dy \quad , \tag{18}$$

where a gauge has been chosen to make $\hat{\mathbf{z}} \cdot \mathbf{A} = 0$ on the photosphere. In our model, photospheric motions consist of horizontal translations $\mathbf{v}_i$ combined with rigid rotations at angular velocity ω_i of the axisymmetric sources. In this case the photospheric helicity flux takes the simple form

$$\frac{dH_R^{(\mathrm{LT})}}{dt} = -\sum_i \frac{\omega_i \Phi_i^2}{2\pi} \; - \; \sum_i \sum_{j \neq i} \frac{\Phi_i \Phi_j}{2\pi} \, \frac{(\mathbf{x}_i - \mathbf{x}_j) \times (\mathbf{v}_i - \mathbf{v}_j) \cdot \hat{\mathbf{z}}}{|\mathbf{x}_i - \mathbf{x}_j|^2} \quad . \tag{19}$$

Figure 14 shows the integral of expression (19) beginning with $H_R(0) = 0$ (the initial field is potential). This compares favorably to the relative helicity of the simulated magnetic field calculated within the simulation domain according to a prescription given in Magara & Longcope (2003).

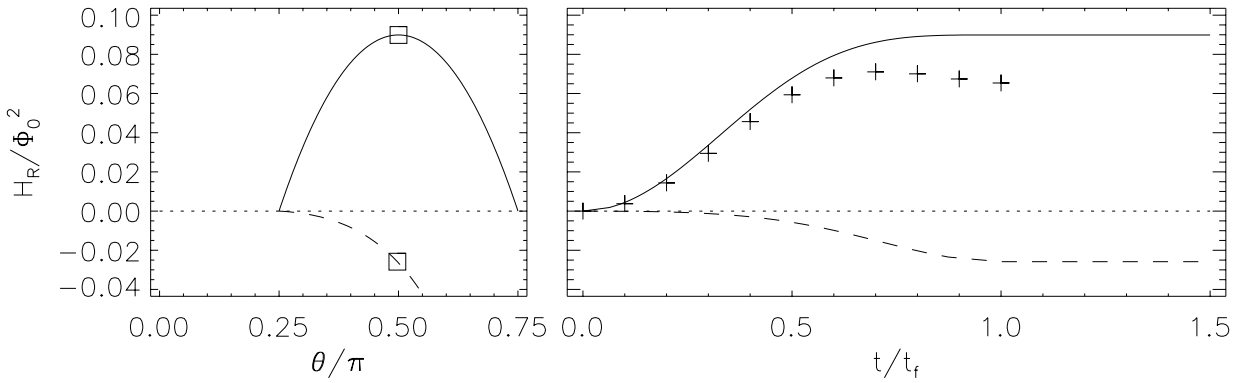

Fig. 14.— The relative helicity injected by photospheric motions. Solid lines show the injected helicity $H_R^{(\mathrm{LT})}$ found by time-integrating expression (19). Dashed curves show $H_R^{(\mathrm{FCE})}$. The left panel shows both *vs.* angle θ and squares denote $\theta = \pi/2$. The right shows the time-history where $\theta(t)$ runs form $= \theta_0 = \pi/4$ to $\pi/2$.

Rather than deduce the footpoint velocities of the FCE we can directly calculate the magnetic helicity of $\mathbf{B}^{(\mathrm{FCE})}$. Introducing an auxiliary field $\mathbf{Z}$ such that $\nabla \times \mathbf{Z} = \mathbf{A}$ for $\mathbf{A}$ in the Coulomb gauge, we integrate (17) by parts[7] to get

$$H_R^{(\mathrm{FCE})} = \int_{z>0} \mathbf{J} \cdot (\mathbf{Z} + \mathbf{Z}_p)\, d\mathbf{x} \;\simeq\; \sum_\sigma 2I_\sigma \int_\sigma \mathbf{Z}_p \cdot d\mathbf{l} \quad , \tag{20}$$

where the final expression, with an integral along each vacuum separator σ, is valid to lowest order in separator currents I_σ. Figure 14 shows the relative helicity of the MCC field (dashed) to be negative and smaller than that injected by the rigid source motions. The negative helicity could have been predicted from the fact that the current on the separator flows in the sense opposite to $\mathbf{B}_p$. The difference $\Delta H_R \equiv H_R^{(\mathrm{LT})} - H_R^{(\mathrm{FCE})}$ between these helicities provides one measure of the discrepancy between the MCC and line-tied evolution.

5.3. Modeling the discrepancy

A simple thought experiment illustrates the potential significance of the discrepancy quantified by ΔH_R. Reversing those *internal* motions which accomplished the energy relaxation $\mathbf{B}^{(\mathrm{LT})} \rightarrow \mathbf{B}^{(\mathrm{FCE})}$ will inject helicity ΔH_R, and will bring the system from $\mathbf{B}^{(\mathrm{FCE})}$ to equilibrium $\mathbf{B}^{(\mathrm{LT})}$. Since the source-region *locations* are fixed during this helicity injection we refer to ΔH_R as the total *self-helicity* of the regions. Following this logic, $H_R^{(\mathrm{FCE})}$, given in expression (20), is the *mutual helicity* quantifying the interlinking of the flux domains about one another. The flux of mutual helicity can be approximated by the double sum in expression (19), which involves relative motions of source pairs. This term is negative in our example since it is dominated by the clockwise rotation of bipole $P1$–$N1$, therefore it is natural that $H_R^{(\mathrm{FCE})} < 0$, as we find.

While the internal footpoint motions taking $\mathbf{B}^{(\mathrm{FCE})} \rightarrow \mathbf{B}^{(\mathrm{LT})}$ will be quite complex, the helicity flux quantifies the overall extent to which footpoints rotate about one another within each source. Due to this overall rotation, the internal footpoint motions will inject *intra-domain* currents which are necessarily absent from $\mathbf{B}^{(\mathrm{FCE})}$. If the motions are smooth within the domain they will inject non-singular current densities, and if they are also localized within the source regions we would expect no net current.

Proceeding along this line, it is possible to estimate the magnitude of current density and excess magnetic energy expected in the line-tied equilibrium $\mathbf{B}^{(\mathrm{LT})}$. The photospheric

[7]Using gauge freedoms in their definitions we make $\hat{\mathbf{z}} \cdot \mathbf{A} = 0$ and $\hat{\mathbf{z}} \times \mathbf{Z} = 0$ on the boundary $z = 0$, eliminating any surface contributions

motions have been designed to leave domains, $P1$–$N1$ and $P2$–$N2$ untwisted, since $P1$–$N1$ is rotated as a whole (all its footpoints are within the disk $r < r_0$) and $P2$–$N2$ is never moved. We therefore expect to find most, if not all, intra-domain current within $P1$–$N2$ and $P2$–$N1$. If we assume that the hypothetical internal motions inject twist into only these domains, leaving footpoints of $P1$–$N1$ and $P2$–$N2$ unaffected, then each domain would receive a self-helicity $\Delta H_R/2$. According to Woltjer's theorem (Woltjer 1958), the magnetic energy in each of these domains is bounded from below by that of a constant-α field: $\nabla \times \mathbf{B} = \alpha_{21}\mathbf{B}$.[8] Motivated by dimensional arguments and axisymmetric cases (see Longcope & Welsch 2000) we approximate the self-helicity $H_{21} \simeq \alpha_{21}\bar{L}_{21}\psi_{21}^2$, where $\bar{L}_{21}$ is the length of a typical field line in the domain. Using this approximation yields a twist value

$$\alpha_{21} \simeq \frac{\Delta H_R}{2L_{21}\psi_{21}^2} \quad . \tag{21}$$

The free energy in each domain can be shown to be $\Delta W_{21} = \alpha_{21}H_{21}/8\pi$. This means that the energy in excess of FCE is at least

$$W_{LT} - W_{FCE} \geq \frac{1}{8\pi}\alpha_{21}\Delta H_R \quad . \tag{22}$$

Figure 15 shows the evolution of α_{21} and $W_{\rm LT}$ over the course of the run. By the end of the simulation the local twist has reached $\alpha_{21} = 0.12/d$, far smaller than the $\alpha \simeq -8/d$ near the simulation's separator. This provides a net current $I_{21} = \alpha_{21}\psi_{21} \simeq 0.06\Phi_0/d$ in each domain. This positive intra-domain current would be distributed throughout $P1$–$N2$ and $P2$–$N1$. Our thought experiment generates this intra-domain current through *internal* motions in each source region. Localized, internal motions are not capable of injecting net currents into a domain, and so there must be opposing, negative current on the separatrices of this region, presumably by discontinuities in the footpoint motions along those separatrices. If the separatrix current were equal and opposite to the total intra-domain current $2I_{21} = 0.12\,\Phi_0/d$, the total inter-domain current would be $\simeq -0.18\Phi_0/d$, close to the observed value in fig. 12.

Figure 15 shows that the self-helicity in each domain boosts the free-energy to $\simeq 6 \times 10^{-4}\Phi_0^2/d$, an order of magnitude greater than the topological energy $\Delta W \simeq 6 \times 10^{-5}\,\Phi_0^2/d$ due to the flux constraints alone.

[8]We use the symmetry of the system to reason that α will be the same in domains $P1$–$N2$ and $P2$–$N1$.

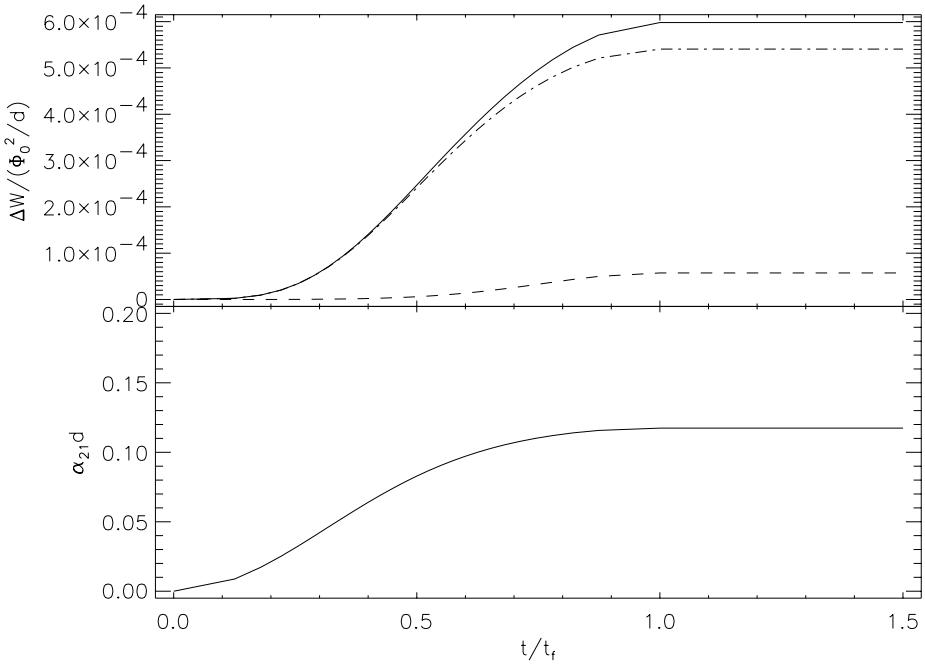

Fig. 15.— An estimate of the energetic consequences of line tying. (bottom) The twist parameter α_{21} corresponding to self-helicity ΔH_R *vs.* time. (top) Estimates of the free energies of $\mathbf{B}^{(\mathrm{LT})}$ (solid) and $\mathbf{B}^{(\mathrm{FCE})}$ (dashed). The dash-dotted line is the lower bound on the excess energy from self-helicity, $W_{\mathrm{LT}} - W_{\mathrm{MCC}}$, from expression (22). The solid line is a sum of this and ΔW_{MCC}, the dashed line.

The free magnetic energy is such a small fraction of the total energy (less than one percent) that it is not possible to reliably compute the free-energy from the simulation. The total magnetic energy within the computational domain is $\sim 0.25\,\Phi_0^2/d$, very close to the energy of the corresponding potential field. Subtracting the two gives an energy difference which peaks at $\sim 3.5 \times 10^{-3}\,\Phi_0^2/d$ some time around $t \simeq 100$, at the same time the photospheric velocity peaks. The system is driven slowly enough that the kinetic energy remains below $2 \times 10^{-3}\,\Phi_0^2/d$, less than 1% of the magnetic energy. Nevertheless, this kinetic energy is almost as large as the difference in magnetic energy. Thus the system must undergo far more viscous relaxation to reach the equilibrium whose energy defines the *free energy* ΔW_{LT}. Were we able to perform this relaxation, we expect that the magnetic energy difference would decrease from its $t = 200$ value of $\simeq 2.3 \times 10^{-3}\,\Phi_0^2/d$. This provides an upper bound to the free energy, which is comfortably far above the theoretical lower bound of $\simeq 6 \times 10^{-4}\Phi_0^2/d$, estimated from the relative helicity.

6. Discussion

We have used two different models to study the quasi-static evolution of coronal fields driven by photospheric field evolution in a simple scenario. In the first model, the Minimum Current Corona, an increasing current flowed along the field's separator as the photospheric sources moved. As the current increased so did the free magnetic energy stored in the field. In the second model, the evolution was found by numerically solving the non-linear, time-dependent equations of ideal MHD subject to line tying. This also showed an increasing current concentration at the separator. In both models the current had the same sense, the same location, and similar time histories. The free magnetic energy stored by line tying was significantly larger than that in the MCC, but not as easily calculated.

The principal difference between the two models was in the presence or absence of continuous currents within the flux domains; so-called intra-domain current. This discrepancy is expected since the two models differ primarily in the footpoint motions they assume. The discrepancy can be quantified through the relative helicity injected by into the corona through the footpoint motions. A piecewise-constant-α field with this helicity provides an estimate of the difference in current and energy between the two models. The estimated separatrix currents more than doubles the magnitude of the inter-domain currents, in agreement with our comparison. It also predicts that the line-tied *equilibrium* field should have a free-energy approximately an order of magnitude larger than the MCC. The magnetic energy in the simulation is larger still, however, much of the excess magnetic energy can be attributed to the field's departure from equilibrium.

This detailed analysis of a simple experiment is intended to shed light on the quasi-static evolution of real coronal fields. While realistic fields will have geometries far more complex than our quadrupole, they will consist of the same geometric components. The MCC can be applied to coronal fields of arbitrary geometric complexity provided they can be approximated by some number of discrete photospheric sources (Longcope & Klapper 2002). Any configuration will, by assumption, evolve through FCEs, which contain current on each and every separator, and nowhere else. Our simple experiment leads us to expect that line-tied, quasi-static evolution of such a field will contain inter-domain currents on the separatrices as well as the separator, and will also contain continuous intra-domain currents in each domain. These additional currents will necessary store additional free energy, since the FCE is a lower-bound on the free-energy of a line-tied field (Longcope 2001). It remains to generalize to more complex fields the technique of estimating free energy using magnetic helicity.

Our comparison was unable to address directly issues of rapid energy release. We can, however, foresee some potential differences between the two models, in this respect. It is easy to quantify the consequences of magnetic reconnection with the MCC by calculating the energy decrease resulting from relaxing (eliminating) one or more constraints. The energy difference depends only on the amount of flux transfered by reconnection, and not on any details of the reconnection such as the local dissipation power density or the electric field. This same mechanism-independence is absent from non-linear, time-dependent MHD simulations, as the wide variety of numerical reconnection studies in the literature demonstrate. Using a current-density sensitive resistivity in nonlinear simulations (Ugai & Tsuda 1977; Sato & Hayashi 1979) is one technique, albeit somewhat *ad hoc*, by which non-linear MHD evolution can transition rapidly between highly-conductive and resistive phases. Simulations of specific solar geometries have used this approach, mostly in two dimensions (Yokoyama & Shibata 1996). In the future, three-dimensional investigations using this technique may provide a numerical comparison to the MCC.

Our analysis, using relative helicity, of the inter-model discrepancy sheds some light on the possibility of rapid energy release following line-tied evolution. Following the transfer of $\Delta\psi$ into domains $P1$–$N1$ and $P2$–$N2$, there will be a lower energy equilibrium to which the field may relax. Quantifying this energy difference would provide an estimate of rapid energy release in the same spirit as the MCC estimate. In both models, the flux transfer will diminish the separator currents, and thereby decrease the equilibrium energy. In the line-tied model it will also re-distribute self-helicities between the domains, permitting a further decrease in energy. The self-helicity will change only on that fraction of field lines which have undergone topological change: $\simeq \Delta\psi/\Psi^{(\mathrm{v})}$. We therefore cannot expect to liberate all of the excess energy W_{LT} from expression (22). Indeed, to liberate the full energy

associated with the small decrease in the self-helicity, $\Delta(\Delta H_R)$, requires Taylor relaxation of entire domain, extending far from the site of reconnection: the separator. This need for additional, internal relaxation after magnetic reconnection has been previously used, with two-dimensional models, to argue that line-tying will inhibit the rapid release of most of a field's free energy (Antiochos et al. 2002). A more detailed calculation of this process, in three dimensions, will be presented in future work.

This material is based upon work supported by the National Science Foundation under grant No. ATM-97227. The numerical computations were carried out using the facilities at the National Center for Atmospheric Research in the US and the National Institute of Fusion Science in Japan.

A. An approximate Current-Flux relationship

This appendix presents an approximate current-flux relationship, $\Psi^{(\mathrm{cr})}(I)$, for equilibrium separator currents. The relationship is derived for small currents which affect the field only in the immediate neighborhood of the magnetic separator of the potential magnetic field. The derivation follows that given by Longcope & Silva (1998), but uses a slightly more concise notation.

A.1. The single line-current approximation

For simplicity we enforce the photospheric boundary conditions by reflecting the coronal field in a mirror corona in the region $z < 0$:

$$B_x(x,y,-z) = B_x(x,y,z) \quad , \quad B_y(x,y,-z) = B_y(x,y,z) \quad , \quad B_z(x,y,-z) = -B_z(x,y,z) \quad .$$

Adding the reflection of the separator field line yields closed curve of length $2L$, which we will denotes $\mathcal{S}$. The first approximation to the separator ribbon is line current I following a closed curve near the separator curve. The actual current path must be chosen so that flux anchored to the sources is topologically unchanged, while an additional self-contained set of field lines wrap around the line current (Longcope & Cowley 1996). For small enough current, however, the current path can be approximated by the potential-field separator and mirror image, $\mathcal{S}$.

We introduce a length coordinate ℓ running along the curve $\mathcal{S}$ in the sense that makes $\mathbf{B} \parallel \hat{\mathbf{l}}$ in the corona. We also introduce the coordinates (ξ, η) within the plane perpendicular

to $\mathcal{S}$ at a given point. Within this plane the perpendicular components of the *potential* magnetic field take the general form

$$B^p_\xi(\rho,\varphi,\ell) \;=\; M_{\xi\xi}\,\rho\cos\varphi \;+\; M_{\xi\eta}\,\rho\sin\varphi \tag{A1a}$$

$$B^p_\eta(\rho,\varphi,\ell) \;=\; M_{\xi\eta}\,\rho\cos\varphi \;+\; M_{\eta\eta}\,\rho\sin\varphi \quad , \tag{A1b}$$

where (ρ,φ) are polar coordinates defined so that $\hat{\boldsymbol{\phi}}$ is right handed with respect to $\hat{\mathbf{l}}$. The coefficients are found from the general Jacobi matrix $M_{ij} = \partial B_i/\partial x_j$, and will depend on ℓ, the coordinate along the separator.

A line current flowing along in the $\hat{\mathbf{l}}$ direction through the origin will add a perpendicular magnetic field $B^I_\varphi = I/2\pi\rho$. Adding this to the potential contribution yields a net azimuthal magnetic field

$$B_\varphi \;=\; B'\rho\cos[2(\varphi-\varphi_0)] \;+\; \frac{I}{2\pi\rho} \quad , \tag{A2}$$

where we have introduced the angle φ_0

$$\tan 2\varphi_0 = -\frac{M_{\xi\xi}-M_{\eta\eta}}{2M_{\xi\eta}}$$

and defined a local magnetic shear

$$B'(\ell) \;=\; \sqrt{\tfrac{1}{4}(M_{\xi\xi}-M_{\eta\eta})^2 + M^2_{\xi\eta}} \;=\; \sqrt{\tfrac{1}{4}T^2 - D} \quad , \tag{A3}$$

where $T = M_{\xi\xi}+M_{\eta\eta} = -\partial B_\ell/\partial\ell$ and $D = M_{\xi\xi}M_{\eta\eta} - M^2_{\xi\eta}$ are the trace and determinant of the two-by-two sub-matrix.[9] This can be expressed without reference to ξ or η using M, the full three-by-three Jacobi matrix, and R, a $\pi/2$ rotation about the local tangent vector $\hat{\mathbf{l}}$,

$$B'(\ell) \;=\; \sqrt{\tfrac{3}{4}(\partial B/\partial\ell)^2 - \tfrac{1}{2}\mathrm{Tr}[\,\mathrm{R}^T\cdot\mathrm{M}\cdot\mathrm{R}\cdot\mathrm{M}\,]} \quad . \tag{A4}$$

The local shear parameter $B'(\ell)$ characterizes the potential magnetic field in the vicinity of the separator. In an axisymmetric field, $\partial/\partial\ell = 0$, the local potential field (A1) may be concisely written in terms of the complex coordinate $\zeta \equiv \xi + i\eta$, as

$$B^p_\eta + iB^p_\xi \;=\; e^{-2i\varphi_0}B'\,\zeta \quad . \tag{A5}$$

This is a classic X-point whose separatrices are inclined from the coordinate axes by an angle φ_0, and B' is the field gradient in its vicinity. Definition (A4) is the natural generalization of this quantity to the vicinity of a separator field line in three dimensions.

---

[9]This expression differs from the definition given in Longcope & Silva (1998), which fails to account for $\partial B_\ell/\partial\ell \neq 0$.

The new field will consist of domains equivalent to those of the potential field plus a domain of field lines wrapping about the current, as in fig. 16. The new domain will be enclosed by two separatrices joined along two separators running roughly parallel to the potential-field separator (see Longcope and Cowley 1996). The distance from $\mathcal{S}$ to the new separator may be estimated by considering the field components in the perpendicular plane, which resemble a classic magnetic island (see fig. 16). The azimuthal field does not reverse direction inside of a radius $\rho_x = \sqrt{|I|/2\pi B'}$, making this a natural estimate of the extent of the wrapping region. Indeed there are two X-type nulls in the transverse field, X_1 and X_2, at angles φ_x satisfying $\cos[2(\varphi_x - \varphi_0)] = -\mathrm{sgn}(I)$. Following X-point X_i as ℓ varies from 0 to $2L$, yield a closed curve $\mathcal{X}_i$ shown fig. 16.[10] For small enough currents these curves will approximate the locations of the two separators, whose true definition cannot be cast in local terms. The innermost of the two separator curves, $\mathcal{X}_{\mathrm{in}}$, will enclose the same flux domains as the potential-field separator, but with a different amount of flux in general.

[10]Due to the reflectional symmetry about $z = 0$ the curves $\mathcal{X}_i$ will not link the central curve, $\mathcal{S}$ or one another.

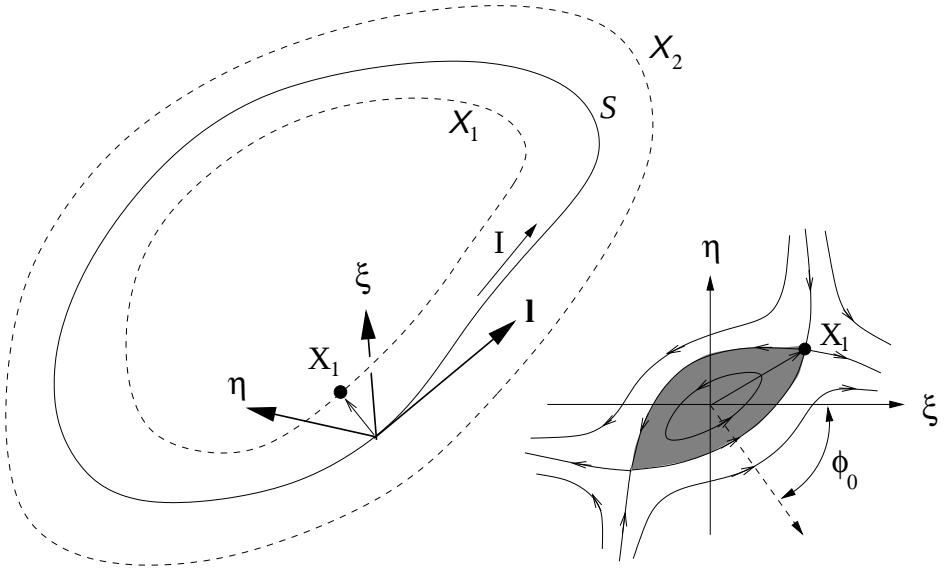

Fig. 16.— The closed curve $\mathcal{S}$ composed of the separator from the potential field and its mirror image. The tangent vector $\hat{\mathbf{l}}$ defines local right-handed coordinate system (ξ, η, ℓ). The inset shows the island-like structure of the field components in the (ξ, η) plane, with two null points, X_1 and X_2. The shaded portion is approximation of the set of field lines which wrap around the line current. The traces of the perpendicular null points form two closed curves, $\mathcal{X}_1$ and $\mathcal{X}_2$.

For this one-line-current approximation of the separator ribbon, the flux Ψ is one-half of that enclosed by curve $\mathcal{X}_{\rm in}$ both in the corona and mirror corona. Including both the flux from the potential field, $\mathbf{B}_p$, and from the current this is

$$2\Psi \;=\; \oint_{\mathcal{X}_{\rm in}} \mathbf{A}_p \cdot d\mathbf{l} \;+\; \frac{I}{4\pi} \oint_{\mathcal{S}} \oint_{\mathcal{X}_{\rm in}} \frac{d\mathbf{l}\cdot d\mathbf{l}'}{|\mathbf{x}-\mathbf{x}'|} \quad . \tag{A6}$$

The double integral in the second term is the well-known Neumann formula for mutual inductance between curve $\mathcal{S}$ (where the current is) and curve $\mathcal{X}_{\rm in}$ (inside which we find the flux).

To evaluate the first integral we note that an integral over the nearby curve $\mathcal{S}$ would be $2\Psi^{(\rm v)}$. The flux within the curve $\mathcal{X}_{\rm in}$, chosen to be *inside* $\mathcal{S}$, will differ by the amount of flux passing between the two curves

$$\oint_{\mathcal{X}_{\rm in}} \mathbf{A}_p \cdot d\mathbf{l} \;\simeq\; 2\Psi^{(\rm v)} \;-\; \int_0^{2L}\int_0^{\rho_x} B^p_\varphi(\rho,\varphi_x,\ell)\,d\rho\,d\ell \;=\; 2\Psi^{(\rm v)} \;+\; {\rm sgn}(I)\int_0^{2L} \tfrac{1}{2}B'\rho_x^2\,d\ell \quad . \tag{A7}$$

The double integral in expression (A6) does not diverge since the curves $\mathcal{S}$ and $\mathcal{X}_{\rm in}$ never intersect. In the limit of very small current, and therefore small separations ρ_x, the two curves are almost parallel and the integral may be replaced by one involving only the current path $\mathcal{S}$ parameterized $\mathbf{x}(\ell)$

$$\oint_{\mathcal{S}} \oint_{\mathcal{X}_{\rm in}} \frac{d\mathbf{l}\cdot d\mathbf{l}'}{|\mathbf{x}-\mathbf{x}'|} \;\simeq\; \int_0^{2L}\int_0^{2L} \frac{\hat{\mathbf{l}}(\ell)\cdot\hat{\mathbf{l}}(\ell')\,d\ell\,d\ell'}{\sqrt{|\mathbf{x}(\ell)-\mathbf{x}(\ell')|^2+\rho_x^2(\ell)}} \quad . \tag{A8}$$

The expression on the right is the self-inductance of a thin wire of radius $\rho_x(\ell)$, which depends on the global geometry of the curve $\mathcal{S}$ as well as on the radius. In the limit $\rho_x \to 0$, where the self-inductance diverges, the two dependences may be formally separated by adding and subtracting the self-inductance of a reference wire with the same divergence. Choosing a circular wire of length $2L$ (major radius L/π) adds and subtracts the contribution

$$\mathcal{L}_\circ(\rho_x) \;\equiv\; \int_0^{2L}\left\{\int_0^{2\pi} \frac{\cos(\theta)\,d\theta}{\sqrt{4\sin^2(\theta/2)+[\pi\rho_x(\ell)/L]^2}}\right\} d\ell \quad , \tag{A9}$$

where $\theta = \pi(\ell'-\ell)/L$. The inner integral may be evaluated in terms of elliptic integrals and, in the limit $\rho_x/L \ll 1$, may be approximated as a logarithm to give

$$\mathcal{L}_\circ(\rho_x) \;=\; \int_0^{2L} \ln\left[\frac{64e^{-4}L^2}{\pi^2\rho_x^2(\ell)}\right] d\ell \;+\; \mathcal{O}(\rho_x^2\ln\rho_x) \quad . \tag{A10}$$

Subtracting the same term from (A8) yields a contribution which converges to a constant at $\rho_x \to 0$. We define this constant as $2L \ln s$,

$$\int_0^{2L}\int_0^{2L} \left\{ \frac{\hat{\mathbf{l}}(\ell)\cdot\hat{\mathbf{l}}(\ell')}{|\mathbf{x}(\ell)-\mathbf{x}(\ell')|} - \frac{\pi\cos[\pi(\ell'-\ell)/L]}{2L|\sin[\pi(\ell'-\ell)/2L]|} \right\} d\ell\, d\ell' \;\equiv\; 2L\,\ln s \quad , \tag{A11}$$

where parameter s characterizes the contribution of the overall geometry of $\mathcal{S}$ to its self-inductance. It is defined to be unity in the case of the reference configuration, a circular loop.

A.2. Matching the two-dimensional current sheet

The analysis to this point has used a single line current, the simplest approximation of a current sheet. Longcope and Cowley describe a method for improving the approximation by increasing the number of line currents until they form the distributed surface current density of a separator current ribbon. Each iteration involves a version of expression of (A6) where the innermost separator $\mathcal{X}_{\rm in}$, has moved and thus there is a new expression for ρ_x. This same technique can be used with a purely axisymmetric field, $\partial/\partial\ell = 0$, in which $\mathcal{S}$ is a ring of X-points. This case can also be approximated by an analytic expression for the current sheet, and thus for the inner separator distance ρ_x. We will use this case to define ρ_x in general, thereby assuring that our current-flux relationship reverts to the analytic expression in cases of axisymmetry.

In the axisymmetric limit, $\partial/\partial\ell = 0$, the local fields may be concisely written in terms of the complex coordinate $\zeta \equiv \xi + i\eta$. The potential field is given by (A5) and a single line current adds $-I/2\pi\zeta$ to this. The so-called Green-Syrovatskii current sheet solution (Green 1965; Syrovatskii 1971) is given by

$$B_\eta + iB_\xi \;=\; e^{-2i\varphi_0} B' \sqrt{\zeta^2 - e^{2i\phi_x}\rho_x^2} \quad . \tag{A12}$$

This is seen to match the potential field (A5) when $|\zeta| \gg \rho_x$. The Cauchy-Riemann conditions of complex analysis (see e.g. Carrier et al. 1966) assure that the field is current-free except along a branch-cut connecting the branch points at $\zeta = \pm e^{i\phi_x}\rho_x$; the branch cut is the current sheet. Integrating around the current sheet yields a net current

$$|I| \;=\; \pi B' \rho_x^2 \quad . \tag{A13}$$

The inner Y-point of the current sheet is therefore located a distance

$$\rho_x = \sqrt{\frac{|I|}{\pi B'}} \tag{A14}$$

from the potential-field separator, a factor $\sqrt{2}$ farther than the X-point in the single-line-current approximation. The total width of this current sheet is twice this distance,

$$\Delta \;=\; \sqrt{\frac{4|I|}{\pi B'}} \quad , \tag{A15}$$

which we adopt as the width of the separator current ribbon.

In order that our general current-flux relationship goes over to a Green-Syrovatskii current ribbon in two dimensions, we adopt expression (A14) in the foregoing analysis. One final modification is to replace the self-flux of a circular line-current with that of a circular ribbon with a surface current distribution following (A12). This modification amounts to replacing the logarithmic factor in expression (A10) with the self-inductance of a current sheet, found as a distribution of line currents at distances ranging from 0 to Δ. Integrating these with the surface current distribution of a Green-Syrovatskii current sheet specifies the transformation

$$\begin{aligned} \ln\left[\frac{64e^{-4}L^2}{\pi^2\rho_x^2}\right] \;\;&\rightarrow\;\; \int_0^1 \ln\left[\frac{64e^{-4}L^2}{\pi^2(u\Delta)^2}\right]\,\frac{8}{\pi}\sqrt{u(1-u)}\,du \\ &=\;\; \ln\left[\frac{64e^{-4}L^2}{\pi^2\Delta^2}\right] \;-\; \frac{16}{\pi}\int_0^1 \ln u\,\sqrt{u(1-u)}\,du \;=\; \ln\left[\frac{256e^{-5}L^2}{\pi^2\rho_x^2}\right] \quad , \end{aligned}$$

after using $\Delta = 2\rho_x$.

Combining expression (A6), (A7) and (A10) and making the substitution above into the self-inductance $\mathcal{L}_\circ$ gives a self-flux

$$\Psi^{(\rm cr)} \;\equiv\; \Psi - \Psi^{(\rm v)} \;=\; \frac{LI}{2\pi} \;+\; \frac{LI}{4\pi}\ln s \;+\; \frac{I}{4\pi}\int_0^L \ln\left[\frac{256e^{-5}L^2B'(\ell)}{\pi|I|}\right]\,d\ell \quad . \tag{A16}$$

Forming the geometric mean of the magnetic shear along the potential-field separator,

$$\bar{B}' \equiv \exp\left\{\frac{1}{L}\int_0^L \ln[B'(\ell)]\,d\ell\right\} \quad , \tag{A17}$$

allows the self-flux to be concisely expressed as

$$\Psi^{(\rm cr)}(I) \;=\; \frac{IL}{4\pi}\ln\left(\frac{256e^{-3}L^2\bar{B}'s}{\pi|I|}\right) \;=\; \frac{IL}{4\pi}\ln\left(\frac{eI^\star}{|I|}\right) \quad , \tag{A18}$$

in terms of the characteristic current[11]

$$I^\star \;\equiv\; \frac{256e^{-4}L^2\bar{B}'s}{\pi} \quad . \tag{A19}$$

[11]Recall that (A19) is in rationalized cgs-emu. The current in cgs-esu is found by multiply the right-hand side by $c/4\pi$, or in MKS by multiplying the right-hand side by μ_0^{-1}.

This definition of $I^\star$ is adopted so that $\partial\Psi^{(\mathrm{cr})}/\partial I = 0$ when $|I| = I^\star$.

In summary, we have derived the flux-current relationship for a separator current ribbon in the limit of small currents. It depends principally on the length L of the separator, and logarithmically on a characteristic current $I^\star$ given by expression (A19). Beyond the current $|I| = I^\star$ the flux-current relationship exhibits an unphysical reversal: larger current produces less flux. The current $I^\star$ depends on the length of the potential field separator as well as two other global properties. The first global parameter, s, characterizes the overall shape the potential field separator according to expression (A11). The second global parameter, $\bar{B}'$, is the geometric mean, as given by (A17), of the local magnetic shear, $B'(\ell)$, in the magnetic shear in the potential field along the separator according to expression (A4).

REFERENCES

Antiochos, S. K., Karpen, J. T., & DeVore, C. R. 2002, ApJ, 575, 578

Baum, P. J., & Bratenahl, A. 1980, Solar Phys., 67, 245

Berger, M. A., & Field, G. B. 1984, JFM, 147, 133

Biskamp, D., & Schwarz, E. 2001, Phys. Plasmas, 8, 4729

Carrier, G. F., Krook, M., & Pearson, C. E. 1966, Functions of a Complex Variable (New York: McGraw-Hill)

Finn, J., & Antonsen, J., T. M. 1985, Comments Plasma Phys. Controlled Fusion, 9, 111

Galsgaard, K., Priest, E. R., & Nordlund. 2000, Solar Phys., 193, 1

Gold, T. 1964, in AAS-NASA Symposium on the Physics of Solar Flares, ed. W. N. Hess (NASA), 389

Gold, T., & Hoyle, F. 1960, MNRAS, 120, 89

Green, R. M. 1965, in Stellar and Solar magnetic fields. Proc. IAU Symp. 22, ed. R. Lust (North-Holland), 398

Klimchuk, J. 2001, in Geophysical Monographs, Vol. 125, Space Weather, 143

Klimchuk, J. A., Sturrock, P. A., & Yang, W.-H. 1988, ApJ, 335, 456

Longcope, D. W. 1996, Solar Phys., 169, 91

Longcope, D. W. 2001, Phys. Plasmas, 8, 5277

Longcope, D. W., & Cowley, S. C. 1996, Phys. Plasmas, 3, 2885

Longcope, D. W., & Klapper, I. 2002, ApJ, 579, 468

Longcope, D. W., & Silva, A. V. R. 1998, Solar Phys., 179, 349

Longcope, D. W., & van Ballegooijen, A. A. 2002, ApJ, 578, 573

Longcope, D. W., & Welsch, B. T. 2000, ApJ, 545, 1089

Low, B. C. 1977, ApJ, 212, 234

Magara, T. 1998, Ph.D. thesis, Kyoto University

Magara, T., & Longcope, D. W. 2003, ApJ, 586, 630

Mikic, Z., Barnes, D. C., & Schnack, D. D. 1988, ApJ, 328, 830

Parker, E. N. 1957, JGR, 62, 509

Priest, E. R., Bungey, T. N., & Titov, V. S. 1997, Geophys. Astrophys. Fluid Dynamics, 84, 127

Sato, T., & Hayashi, T. 1979, Physics of Fluids, 22, 1189

Sweet, P. A. 1958a, in Electromagnetic Phenomena in Cosmical Physics, ed. B. Lehnert (Cambridge, U.K.: Cambridge University Press), 123

Sweet, P. A. 1958b, Nuovo Cimento, 8, 188

Syrovatskii, S. I. 1971, Sov. Phys. JETP, 33, 933

Ugai, M., & Tsuda, T. 1977, J. Plasma Phys., 17, 337

Woltjer, L. 1958, Proc. Nat. Acad. Sci., 44, 489

Yokoyama, T., & Shibata, K. 1996, PASJ, 48, 353

Zhang, M., & Low, B. C. 2001, ApJ, 561, 406

This preprint was prepared with the AAS LaTeX macros v5.2.